The small-amplitude dynamics of spontaneous tropical cyclogenesis

Hao Fu* and Morgan O'Neill
Department of Earth System Science, Stanford University

* Email: haofu736@gmail.com

This is a preprint for EarthArXiv. The manuscript has been submitted to *Journal of the Atmospheric Sciences*. Subsequent versions may have slight modifications. The authors welcome feedback from anyone who reads the manuscript.

The small-amplitude dynamics of spontaneous tropical cyclogenesis

Hao Fu,[a] Morgan O'Neill,[a]

[a] *Department of Earth System Science, Stanford University, California*

Corresponding author: Hao Fu, haofu736@gmail.com

ABSTRACT: Cloud-permitting simulations have shown that tropical cyclones can form spontaneously in a quiescent environment with uniform sea surface temperature. While the moisture-radiation instability is known as the main mechanism for early-stage growth, two key questions remain unresolved: First, how does the noisy cumulus cloud field organize into a mesoscale perturbation? Second, what determines the length scale of the growing perturbation? This paper develops a theoretical framework in the spectral space to understand the mesoscale perturbation produced by homogeneous random convection and its amplification with mesoscale instability. The theory assumes that the random stretching of planetary vorticity by homogeneous random convection produces the initial vorticity perturbation. The theory predicts that the magnitude of its mesoscale component is universally proportional to the square root of the domain-averaged accumulated rainfall, in agreement with cloud-permitting simulations. The perturbation then kicks off a mesoscale instability that features exponential growth. The instability has a most unstable wavelength. Linear stability analysis shows that the most unstable wavelength is proportional to the geometric mean of the effective Rossby deformation radius of the convectively coupled gravity wave and a ~ 10 km convective spreading length scale. Mechanism-denial numerical experiments show that the convective spreading length scale depends on the spread of convective activity by cold pools and the nonlocal longwave radiative heating induced by anvil clouds.

1. Introduction

Tropical cyclogenesis is a multiscale fluid dynamical process with multiple stages. A clean tool for studying tropical cyclogenesis is the rotating radiative-convective equilibrium (RRCE) setup (Bretherton et al. 2005; Nolan et al. 2007; Khairoutdinov and Emanuel 2013; Wing et al. 2016; Muller and Romps 2018; Carstens and Wing 2020; Yang and Tan 2020; Ramírez Reyes and Yang 2021; Carstens and Wing 2020, 2022). The RRCE is an idealized cloud-permitting simulation configuration that sets a uniform sea surface temperature in a doubly periodic domain, without background wind. This setup isolates the basic internal instability of rotating moist convection at a price of excluding the more realistic tropical cyclogenesis paths that involve a synoptic-scale disturbance such as the easterly wave and its breaking (Gray 1998; Dunkerton et al. 2009), or the roll-up of the Intertropical Convergence Zone (ITCZ) (Narenpitak et al. 2020), etc.

Spontaneous tropical cyclogenesis at the early stage has been qualitatively explained as the mutual enhancement between convection and the secondary circulation induced by diabatic heating. The secondary circulation has an inflow branch at the midlevel (~ 5 km) and an outflow at the upper level (~ 10 km) (Ruppert et al. 2020). It has two main roles:

- First, the secondary circulation may directly lift vapor and liquid water and enhance the condensation and frozen heating in the saturated midlevel region (Yang and Tan 2020) or near the boundary layer top (Lindzen 1974). Suppose the latent heating is strong enough to overcome the stable stratification. In that case, the system will self-amplify like an unstable inertial gravity wave with an imaginary buoyancy frequency and therefore resemble rotating Rayleigh-Bénard convection in the laboratory (Chandrasekhar 1961; Boubnov and Golitsyn 1986). It remains unclear whether the latent heating is strong enough to overcome the stable stratification. Mathematically, this is equivalent to the wave-CISK model (wave-induced conditional instability of the second kind) (Lindzen 1974; Dunkerton and Crum 1991; Liu et al. 2019; Yang 2020).

- Second, the secondary circulation may moisten the environment (Sobel et al. 2001; Derbyshire et al. 2004; Bretherton et al. 2004). This mechanism depends critically on the height of the inflow layer, which is at the midlevel for a typical top-heavy vertical velocity profile. Because the midlevel moist static energy is low, the inflow draws in low moist static energy air and dries the air column, disfavoring future convection. The concept “effective gross moist stability" is introduced to measure the net moistening of an air column in response to a given convergent forcing, in analogy to the dry static stability (Neelin and Held 1987; Raymond and Sessions 2007; Raymond et al. 2009; Fuchs and Raymond 2017). Unlike wave-CISK, this moisture-dependent convective feedback (named moisture mode) requires the free-tropospheric vapor as a memory variable. [1]

The longwave radiative feedback has been shown to accelerate tropical cyclogenesis significantly (Davis 2015; Wing et al. 2016; Muller and Romps 2018; Yang and Tan 2020; Ruppert et al. 2020). It enhances both the wave-CISK and the moisture instability. Deep convection’s anvil clouds trap longwave radiation and induce a warm anomaly in the convective region, producing a radiation-driven secondary circulation. On the one hand, the secondary circulation can directly amplify latent heating in the middle- and upper-level saturated air layer (Yang and Tan 2020) or near the boundary layer top. We call it “wave-CISK-radiation instability". On the other hand, because the longwave heating anomaly projects onto the full depth of the troposphere, the secondary circulation is more bottom-heavy. It transports more vapor to the convective region, reducing the effective gross moist stability (Ruppert et al. 2020; Ruppert 2022). We call it “moisture-radiation instability".

Despite the progress in identifying the key physical factors, there are two critical questions:

- All of the above feedback must work on an existing mesoscale perturbation. How does the noisy convection produce the initial mesoscale disturbance?
- What determines the length scale of the growing mesoscale perturbation? Is there a most unstable wavelength?

For the first question, we are unaware of any theory that predicts the vorticity fluctuation produced by quasi-homogeneous deep convection. Previous works show that a nonuniform water vapor or vorticity field can be produced by random convective events (Hottovy and Stechmann 2015; Fu and O’Neill 2021). These anomalies do not quickly disappear after an individual convective event finishes, and random places can receive multiple updrafts to become a moist and high-vorticity region. In idealized models of column water vapor, convection has been treated as white noise

[1]Mathematically, this is close to the Ekman-CISK model, where the low-level vorticity induces Ekman pumping that makes the moist air from the boundary layer condense and further spin up the vorticity (Charney and Eliassen 1964; Ooyama 1969; Schecter and Dunkerton 2009). The vorticity does not vanish after the convective stretching, so it also serves as a memory variable. However, Ekman-CISK is only a mathematical analogy to the moisture mode. This is because there is very little low-level vorticity and Ekman pumping at the early stage of spontaneous tropical cyclogenesis.

(Hottovy and Stechmann 2015; Ahmed and Neelin 2019). However, this approach neglects a critical property: deep convection is an intermittent and local event that only takes a small fractional area. Mapes (1997) proposed that a red noise spectrum with lower amplitude at the high horizontal wavenumber end is more realistic. This paper theoretically derives the vorticity's wavenumber spectrum produced by intermittent stochastic convection.

For the second question, previous works focus on deriving the spectral growth rate (the growth rate of different scales of perturbation) without invoking any horizontal diffusion or with an artificial diffusion whose physical origin is unclear. For an inviscid and non-diffusive primitive equation, wave-CISK renders the highest growth rate at the highest horizontal wavenumber, which is unrealistic (Ooyama 1982; Dunkerton and Crum 1991). For a system with a negative effective gross moist stability (and Ekman-CISK), the growth rate flattens at the high wavenumber end (Charney and Eliassen 1964; Fuchs and Raymond 2002). This is less problematic than the wave-CISK, but it still predicts the fastest growth at the cloud scale and does not predict any length scale. Thus, it is still incomplete. As a result, some researchers argue that the cloud-scale "microscopic" processes, such as gravity waves (Mapes 1993; Brenowitz et al. 2016; Yang 2020), cold pools (Windmiller and Craig 2019; Yang et al. 2021), cloud lateral expansion (Windmiller and Craig 2019), and water vapor lateral mixing (Craig and Mack 2013) could serve as diffusive factors that suppress the high wavenumber growth of tropical convective systems in general. However, whether the cloud-scale processes indeed serve as a mesoscale diffusivity has not been carefully testified with full-physics cloud-permitting simulations, and whether it can help explain the length scale of spontaneous tropical cyclogenesis remains unclear.

In this paper, we use cloud-permitting simulations to show that increasing the sub-cloud rain evaporation rate can increase the size of an early-stage mesoscale vortex. This motivates us to prescribe the diabatic heating to be proportional to the spatially smoothed tropospheric water vapor content with a Gaussian filter. This idea is similar yet different from Brenowitz et al. (2016), who let the diabatic heating be equal to the filtered low-level divergence instead (wave-CISK) and did not consider the Coriolis force. Applying this filter formulation to a linear stability analysis of a rotating stratified atmosphere with moisture-radiation instability, we obtain the growth rate for different wavenumbers, which agree well with the cloud-permitting simulations. The wavelength of the most unstable mode is proportional to $(L_R L_c)^{1/2}$, where L_R is the effective Rossby deformation radius of the first baroclinic mode convectively coupled gravity waves, and L_c is the bulk convective spreading length scale which is used for smoothing the diabatic heating term. The mismatch of the growth rate between the simulation and the wave-CISK-radiation model rules out the wave-CISK-radiation instability. However, the wave-CISK-radiation feedback could effectively reduce the wave speed of the convectively coupled wave and therefore reduce L_R. The physical processes we study in this paper are illustrated in Fig. 1.

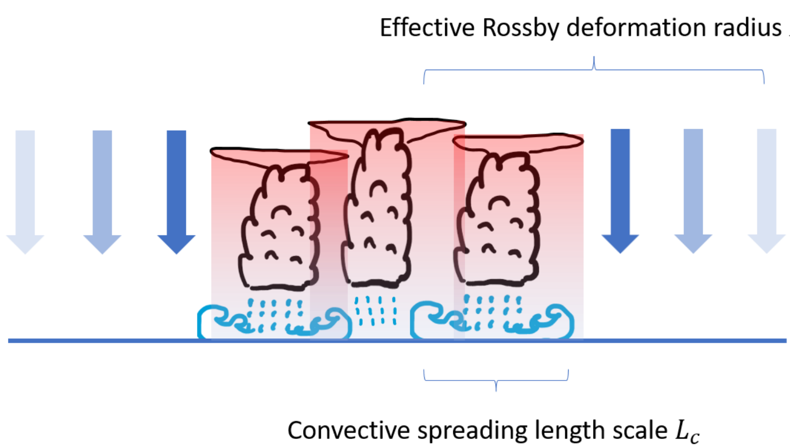

Fig. 1. A schematic diagram of some critical physical processes in spontaneous tropical cyclogenesis. In the region with more vigorous convection, there is more latent heat release and more longwave radiative heating. This drives a secondary circulation that could enhance latent heat release by providing more moisture (moisture-radiation feedback) or directly causing more saturated ascent (wave-CISK-radiation feedback). The effective Rossby deformation radius L_R sets a long-wavelength cutoff for the system's most unstable wavelength. This paper shows that the spread of convective activity by cold pools and the nonlocal radiative effect produced by the anvil cloud could render a convective spreading length scale L_c, which sets a short-wavelength cutoff.

The paper is organized in the following way. Section 2 introduces the numerical simulation setup and the experimental design. Section 3 analyzes the numerical experimental results. Section 4 introduces the theoretical model. Section 5 concludes the paper. A derivation note, the tables of mathematical symbols, simulation movies, and some computing codes are deposited in the supplemental material.

2. Numerical simulation Setup

We perform full-physics cloud-permitting simulations using the Bryan Cloud Model 1 (Bryan and Fritsch 2002) with a 1080×1080 km^2 doubly periodic domain on an f-plane. There are $576 \times 576 \times 65$ grid points and a horizontal grid spacing of 2 km. The model top is a lid at 28 km height, and Rayleigh damping is imposed on the grids above 20 km to dampen reflective gravity waves. The vertical grid is refined at the lower level, with eight vertical layers in the lowest 1 km. A fixed sea surface temperature of 300 K is used. The initial sounding is the horizontal average of a 120×120 km^2 small-domain non-rotating simulation running to the end of day 100, so it is approximately in radiative-convective equilibrium. Some random perturbations of potential temperature at the lowest five levels with a maximum amplitude of 0.1 K are added to the initial condition. The model uses Morrison double moment cloud microphysics scheme (Morrison et al. 2005), RRTMG radiation transfer scheme (Clough et al. 2005) (the solar constant is reduced to 650.83 W m^{-2}, and the zenith angle is fixed at 50.5° to remove the diurnal cycle, following Bretherton et al. (2005)), the simple planetary boundary layer scheme by Bryan and Rotunno (2009), and a surface layer model based on the similarity theory ("sfcmodel=3" in the namelist file, Jiménez et al. 2012).[2]

We perform four groups of experiments that 1) change the Coriolis parameter, 2) change the magnitude of the horizontal anomaly of longwave radiative heating rate, 3) change the sub-cloud rain evaporation rate, and 4) smooth the horizontal anomaly of longwave heating rate. The experiments' spin-up stage is used to validate the theory of cloud-generated vorticity fluctuation. The subsequent exponential growth stage is used to inspire and benchmark the theory of mesoscale instability.

For Group 1, the aim of varying the Coriolis parameter f is to provide a set of general tests. The sensitivity to f for the most unstable growth rates of the moisture-radiation instability and the wave-CISK-radiation instability is drastically different, so we use it to identify which mechanism is at work.

For Group 2, the aim of varying the horizontal longwave heating anomaly is to directly control the strength of longwave radiative feedback. To modify the horizontal longwave heating anomaly, we multiply the horizontal anomaly of the variable "lwten" (unit: K s^{-1}, in the script "radia-

[2]This setting is close to the configured "testcase=8: Radiative-Convective Equilibrium" test. The only difference is the surface layer model. The configured setting uses "sfcmodel=1" which yields an overly low surface heat flux.

tion_driver.F") by a parameter RAD, and then reconstruct the variable "lwten" by summing up the anomaly and the horizontally averaged part. Previous numerical studies have turned on and off the horizontal anomaly of longwave radiative heating (e.g., Yang and Tan 2020; Ramírez Reyes and Yang 2021). However, we are unaware of any previous simulation that multiplies it with a prescribed number. This provides a more quantitative way to examine the role of longwave radiative feedback.

For Group 3, the aim of varying the sub-cloud rain evaporation rate is to study the sensitivity of the most unstable mode's growth rate and wavelength to cold pools. A cold pool is analogous to a wave emitted by convection. It can nonlocally trigger convection by lifting the mixed layer parcels to the level of free convection (Grandpeix and Lafore 2010; Meyer and Haerter 2020), or by gaining vapor and heat via wind-induced surface heat flux and transporting it to the neighboring convective site (Tompkins 2001; Langhans and Romps 2015; Windmiller and Craig 2019; Jensen et al. 2022). We multiply the inverse of rain evaporation time scale in the microphysics scheme (parameter EPSR in "morrison.F" file) by a parameter E_v. Only the rain evaporation rate in the lowest 500 m of the domain is modified. Modulating rain evaporation rate is a standard way to study the role of cold pools (Jeevanjee and Romps 2013; Wang et al. 2019; Nissen and Haerter 2021; Fu and O'Neill 2022). These previous studies focus on whether the cold pools suppress or enhance mesoscale instability, not how cold pools influence the length scale of a growing mesoscale disturbance.

For Group 4, the aim is to indirectly study the nonlocal radiative effect of anvil clouds. The anvil cloud is much wider than the updraft core, so the anomalous radiative heating region is also wider (Nolan et al. 2007). We ask whether this nonlocal behavior of radiative feedback can influence the system's most unstable wavelength. One way to manipulate the anvil cloud size is to tune the ice sublimation rate (Seeley et al. 2019). However, as we focus on the influence of nonlocal radiative heating on the vortex length scale, a simpler way is to mimic the expansion of anvil clouds by directly smoothing the longwave heating tendency. We are particularly interested in how the filtering scale shifts the most unstable wavelength. For example, does a 10-km scale Gaussian filter increase the most unstable wavelength by only 10 km? This experiment could reveal the basic dynamics of the instability. In practice, we filter the longwave heating tendency (variable "lwten" in CM1, unit: K s^{-1}) with a 2D Gaussian filter: [3]

$$\widetilde{A_{l_{filter}}} \equiv \frac{1}{\pi l_{filter}^2} \iint \exp\left(-\frac{|\mathbf{x}-\mathbf{x}'|^2}{l_{filter}^2}\right) A(\mathbf{x}', z, t) d\mathbf{x}', \tag{1}$$

where A is any three-dimensional scalar, l_{filter} is an arbitrary filter length, $\mathbf{x}$ is the horizontal position vector, z is height above the sea level, t is time. We let the artificial radiative filter length be $l_{filter} = l_{rad} = 0$ km, 12 km, and 24 km.

The reference test has $f = 10^{-4}$ s^{-1} (equivalent to 42°N) and RAD = 2. The motivation for using such a high Coriolis parameter is to suppress the stationary gravity waves that would otherwise occur in a lower Coriolis parameter test and add complexity to the numerical experiments. The stationary gravity waves are unrealistic phenomena associated with the doubly periodic boundary condition. The motivation for doubling the horizontal anomaly of longwave heating is to make the signal of longwave radiation feedback stand out from other feedback and the convective noise. It also accelerates tropical cyclogenesis and saves computational resources. For each experiment, we perform three tests. We change one parameter at a time. The experiments are summarized below and in Table 1:

- For Group 1, we have $f = 0.25 \times 10^{-4}$ s^{-1}, $f = 0.5 \times 10^{-4}$ s^{-1}, and $f = 1.0 \times 10^{-4}$ s^{-1}.
- For Group 2, we have RAD = 1.0, RAD = 1.5, and RAD = 2.0.
- For Group 3, we have $E_v = 0.5$, $E_v = 1.0$, and $E_v = 1.5$.
- For Group 4, we have $l_{rad} = 0$ km, $l_{rad} = 12$ km, and $l_{rad} = 24$ km.

Note that the $f = 1.0 \times 10^{-4}$ s^{-1} (Group 1), RAD = 2.0 (Group 2), $E_v = 1.0$ (Group 3), and $l_{rad} = 0$ km (Group 4) tests are the same and are identical to the reference test. As a clarification, we do not discuss shortwave radiative feedback in this paper, and any "radiative feedback" denotes longwave radiative feedback.

[3]The implementation of this radiative filter is not trivial for parallel computation, because most atmospheric models (including CM1) use halo layers to communicate data between processors. As the radiative filter is a nonlocal operation, its direct implementation requires tens of halo layers, drastically increasing the computing time. Our idea is to decompose the filter into a series of local finite-difference Fickian diffusion steps, which converge to the Gaussian filter, given that each step is small. See the supplemental material for a script that can be inserted into the standard CM1 code.

TABLE 1. The parameters of the mechanism-denial numerical experiments

Name	f (s^{-1})	RAD	E_v	l_{rad} (km)
Reference	10^{-4}	2	1	0
Group 1-A	0.25×10^{-4}	2	1	0
Group 1-B	0.5×10^{-4}	2	1	0
Group 2-A	10^{-4}	1	1	0
Group 2-B	10^{-4}	1.5	1	0
Group 3-A	10^{-4}	2	0.5	0
Group 3-B	10^{-4}	2	1.5	0
Group 4-A	10^{-4}	2	1	12
Group 4-B	10^{-4}	2	1	24

3. Experimental results

a. Basic flow statistics and pattern

First, we introduce the basic flow statistics and patterns, which provide a physical picture. For the reference test, Fig. 2a shows that the surface wind of the mesoscale vortex outweighs that associated with the gust front by day 12, which is a sign of the surface vortex spin up. The surface vortex induces a more substantial surface heat flux and leads to more substantial precipitation (Fig. 2b). A smaller RAD significantly delays the surface vortex formation but does not influence the gust front wind and precipitation before day 12.

Figure 3 shows the time evolution of the midlevel vorticity (z = 5.25 km) and the upper-level vorticity (z = 10.25 km) of the reference test. At the midlevel, a regular pattern of cyclones and anticyclones grows out of the noisy vorticity pattern by day 4. The convection-induced stretching and tilting of vortex tubes produce a noisy vorticity pattern. Figure 4a and b show the vertical profile of the mesoscale vorticity and vertical velocity calculated by sub-domain averaging (see the caption for details). At the relatively moist region where the mesoscale vertical velocity is positive, the mid-level is cyclonic and the upper-level is anticyclonic. This is mainly produced by stretching planetary vorticity at the middle level and squashing planetary vorticity at the upper level, and vice versa for mesoscale descents in the relatively dry region. There is little mesoscale vertical motion below 5 km height due to the rough cancellation between the condensation heating and rain evaporative cooling (Fig. 5b).

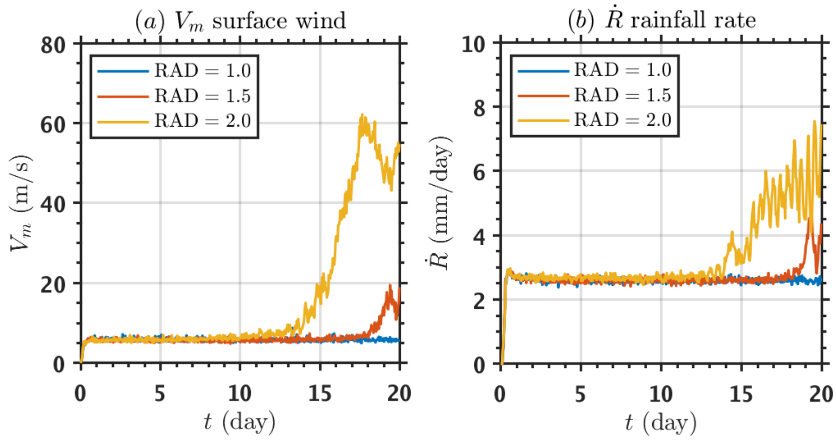

FIG. 2. (a) The surface maximum wind (unit: m s^{-1}) of the RAD = 1.0 test (the blue line), the RAD = 1.5 test (the red line), and the RAD = 2.0 test (the orange line) which is the reference test. (b) the same as (a), but for the domain-averaged surface rainfall rate $\dot{R}$ (unit: mm day^{-1}). The sampling (model output) time interval is 1 hour.

Then, we analyze the longwave radiative heating rate. The longwave heating rate's horizontal anomaly at the relatively moist region takes a roughly constant positive value below 10 km height. It has a negative spike at around 11.5 km height due to the cloud top emission (Fig. 5c). The vertical shape of the longwave heating tendency indicates that the radiation-driven component of the secondary circulation should have a low inflow level and favors the aggregation of water vapor (Ruppert et al. 2020). We define the ratio of the density-weighted $z = 0.025 - 10.25$ km vertically averaged horizontal anomaly of longwave radiative heating rate to that of the latent heating rate as the "cloud-radiative parameter": ϵ_{rad}, which is averaged between the 25% moistest and the 25% driest boxes. The reference test has doubled the radiative feedback and yields $\epsilon_{rad} \approx 0.9$. Figure 6 shows that the ϵ_{rad} increases with RAD. [4]

After day 4, the horizontal pattern of vorticity actively evolves. The vorticity of the midlevel vortices keeps amplifying, and the vortex size grows by merging (Fig. 3). The vertical structure of

[4]In idealized tropical wave models, people have used $\epsilon_{rad} = 0.15$ (Fuchs and Raymond 2002) and $\epsilon_{rad} = 0.17$ (Fuchs and Raymond 2017; Wang and Sobel 2022), but they did not justify the choice from observations or cloud-permitting simulations.

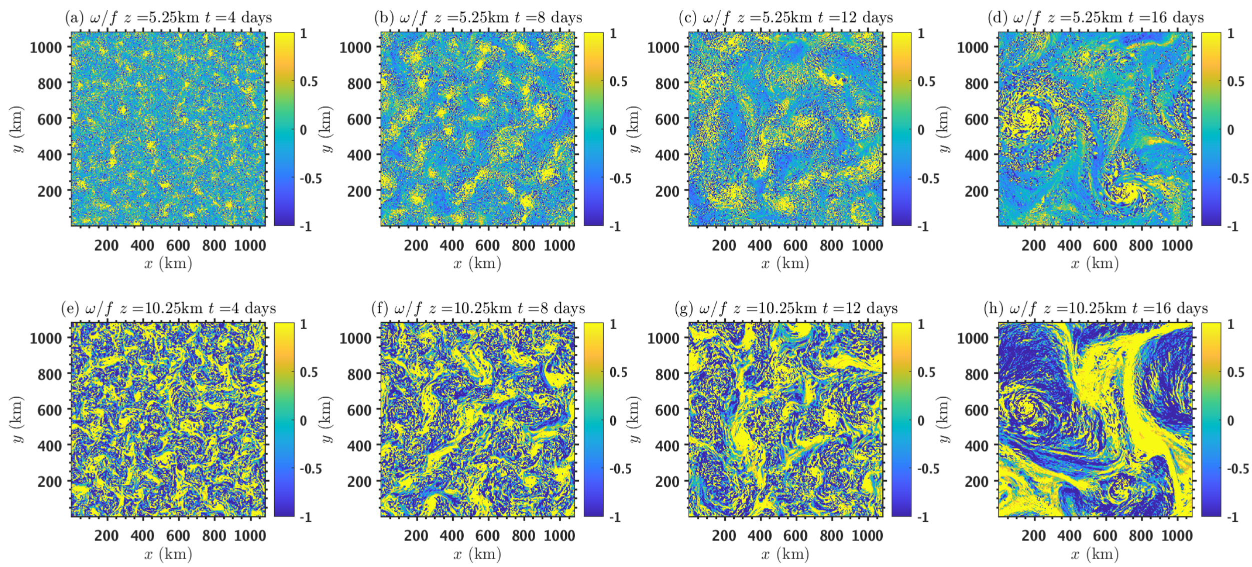

FIG. 3. The vertical relative vorticity normalized by f for the reference test. (a)-(d) show the $z = 5.25$ km field at $t = 4$ days, $t = 8$ days, $t = 12$ days, and $t = 16$ days. (e)-(h) show the $z = 10.25$ km field.

the vertical vorticity also evolves. On day 16, the vortices are cyclonic at both the middle and the upper levels. This bias to cyclone could be a finite-amplitude effect (Fu and Sun 2021) that will not be further studied in this paper.

b. The spin up stage and exponential growth stage

We use the standard deviation (std) of the 20 km Gaussian filtered ($l_{filter} = 20$ km) midlevel ($z = 5.25$ km) vertical vorticity (denoted as $\widetilde{\omega_{20km}}$) to more quantitatively track the system evolution. The 20 km filter aims to smooth the cloud-scale fluctuation without meaningfully affecting the mesoscale property. Figure 7(a)-(d) show an initial spin-up stage between day 0 and day 2 where the std($\widetilde{\omega_{20km}}$) grows rapidly. The system smoothly transitions to an exponential growth stage roughly between day 2 and day 4.

Figure 7(e)-(h) plot the std($\widetilde{\omega_{20km}}$) versus the domain-averaged accumulated rainfall R (unit: mm) in a log-log coordinate during the spin-up stage, which clearly shows:

$$\mathrm{std}(\widetilde{\omega_{20km}}) \sim R^{1/2}. \tag{2}$$

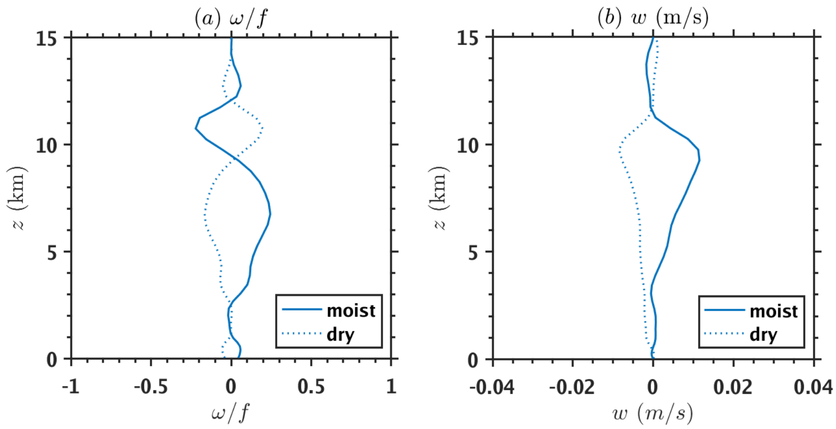

FIG. 4. The vertical profiles of the sub-domain (a) vertical vorticity (normalized by f), (b) vertical velocity (unit: m s^{-1}) for the reference test at $t = 4$ days. In calculating the profiles, the domain is first divided into 36 km $\times$ 36 km blocks. The blocks are ranked by their average column precipitable water (unit: m). The solid lines show the average quantities of the 25% of blocks with the highest column precipitable water, and the dotted lines show the 25% of blocks with the lowest column precipitable water.

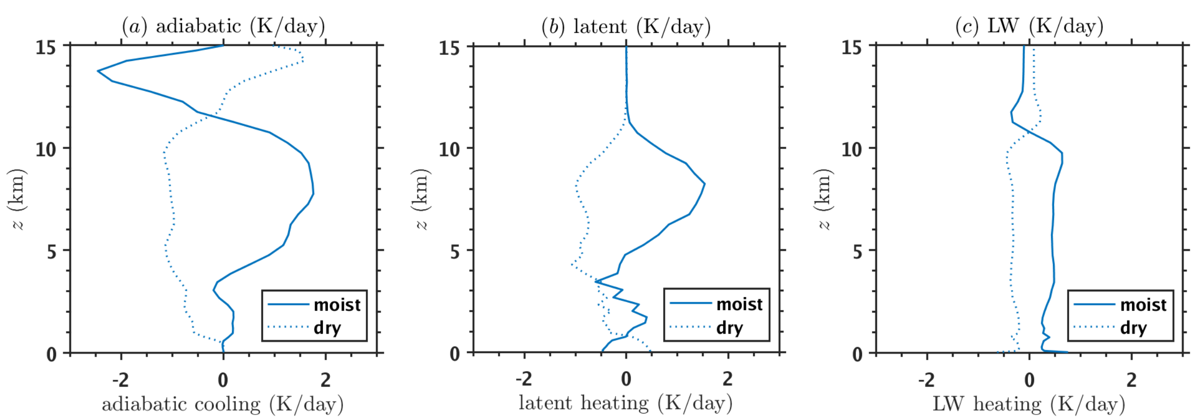

FIG. 5. The same as Fig. 4, but for (a) the horizontal anomaly of adiabatic cooling rate (unit: K day^{-1}, the vertical advection of the background potential temperature multiplied with a minus sign), (b) the horizontal anomaly of latent heating rate (unit: K day^{-1}), and (c) the horizontal anomaly of longwave radiative heating rate (unit: K day^{-1}) for the reference test at $t = 4$ days.

The accumulated rainfall R, which is the integral of the domain-averaged precipitation rate $\dot{R}$ (unit: mm day^{-1}) shown in Fig. 2b, measures the accumulated convergence induced by convection. The

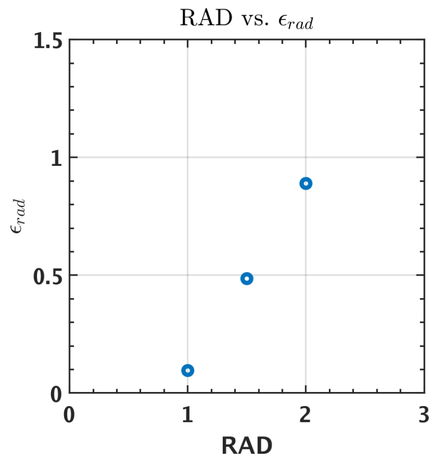

FIG. 6. The ϵ_{rad} (the magnitude ratio of longwave radiative heating anomaly to latent heat) versus RAD (the parameter multiplied on the horizontal anomaly of longwave radiative heating term in CM1) at day 4.

$\dot{R}$ is also a measure of the tropospheric overturning strength, which climbs up from zero rapidly and stays around an equilibrium value afterward. Because R is monotonic to time, it is viewed as a rescaled time coordinate. In section 4b, we rigorously prove (2) by considering the vorticity produced by deep convection as a random superposition problem.

The subsequent exponential growth shown in Fig. 7 indicates a linear instability process. The sensitivity to f, RAD, E_v, and l_{rad} are qualitatively analyzed below, with a particular emphasis on the vortex length scale. In section 4c, we will show the spectral growth rate, which provides more quantitative information.

c. Sensitivity to the Coriolis parameter

The first row of Fig. 8 shows the midlevel vertical vorticity ω normalized by f for Group 1. The cloud-scale vorticity dipoles produced by tilting make the signal-to-noise ratio smaller for a test with smaller f (e.g., Fig. 8a). Thus, we let the second row of Fig. 8 show the vorticity smoothed with a 20 km Gaussian filter ($\widetilde{\omega_{20km}}$).

The magnitude of $\widetilde{\omega_{20km}}/f$ increases as f decreases. This is primarily due to the slightly higher magnitude of the normalized perturbation produced at the spin-up stage (Fig. 7a and e), which may involve contributions from vorticity dipoles produced by tilting. No significant change in the vortex length scale can be identified by eye.

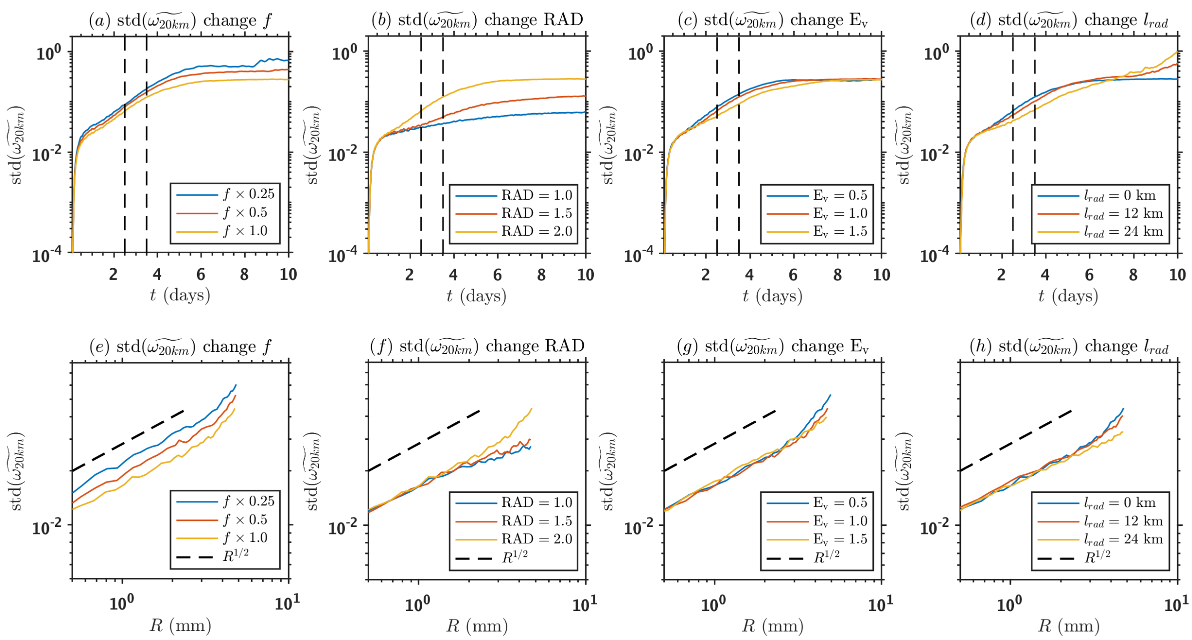

FIG. 7. The standard deviation of the 20 km filtered vorticity $\widetilde{\omega_{20km}}$. The upper row plots its evolution with time, with std($\widetilde{\omega_{20km}}$) in a log coordinate. The lower row plots its evolution with the domain-averaged accumulated rainfall R in a log-log coordinate, and the time series is truncated at $t = 2$ days (day 2). The first column shows the Group 1 experiments, with the blue lines denoting the $f = 0.25 \times 10^{-4}$ s^{-1} test, the red lines denoting the $f = 0.5 \times 10^{-4}$ s^{-1} test, and the orange lines denoting the $f = 10^{-4}$ s^{-1} test. The second column shows the Group 2 experiments, with the blue lines denoting the RAD = 1.0 test, the red lines denoting the RAD = 1.5 test, and the orange lines denoting the RAD = 2.0 test. The third column shows the Group 3 experiments, with the blue lines denoting the $\mathrm{E_v} = 0.5$ test, the red lines denoting the $\mathrm{E_v} = 1.0$ test, and the orange lines denoting the $\mathrm{E_v} = 1.5$ test. The fourth column shows the Group 4 experiments, with the blue lines denoting the $l_{rad} = 0$ km test, the red lines denoting the $l_{rad} = 12$ km test, and the orange lines denoting the $l_{rad} = 24$ km test. The vertical dashed black lines in the upper row mark the $t = 2.5$ days and $t = 3.5$ days time which render the time slot used in diagnosing the growth rate (Fig. 14). The dashed black lines in the lower row are the $R^{1/2}$ reference lines. The sampling (model output) time interval is 1 hour.

d. Sensitivity to the longwave radiative feedback strength

Figure 9 shows the midlevel vorticity for Group 2. The magnitude of ω/f increases significantly with RAD, in agreement with the strong sensitivity of the genesis process to the longwave radiative

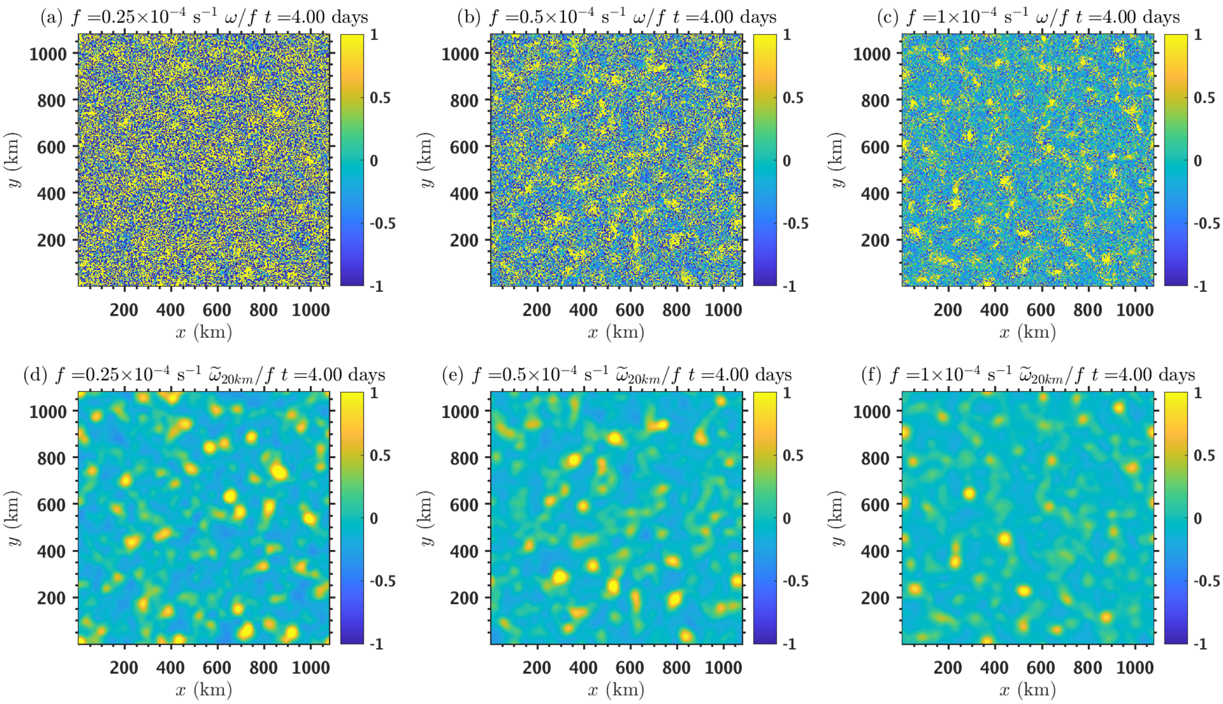

FIG. 8. Some snapshots at $t = 4$ days for Group 1 (changing the Coriolis parameter). The first row is the $z = 5.25$ km (midlevel) relative vertical vorticity normalized by f for (a) the $f = 0.25 \times 10^{-4}$ s^{-1} test, (b) the $f = 0.5 \times 10^{-4}$ s^{-1} test, (c) the $f = 1 \times 10^{-4}$ s^{-1} test. The second row is the 20 km filtered field of the first row.

heating reported in previous works (Wing et al. 2016; Muller and Romps 2018; Yang and Tan 2020). No significant change in the vortex length scale can be identified by eye.

e. Sensitivity to the sub-cloud rain evaporation

Figure 10 shows that a higher sub-cloud rain evaporation rate makes the mesoscale vortices larger and weaker. Stronger sub-cloud rain evaporation makes cold pools stronger, which makes the initiation of convection depend more on the gust front produced by neighboring clouds. In this way, clouds rarely form alone.

f. Sensitivity to the filter on longwave radiative heating

Figure 11 shows that a larger-scale filter on the longwave heating tendency makes the mesoscale vortices larger and weaker. Surprisingly, even an $l_{rad} = 12$ km filter can significantly increase the

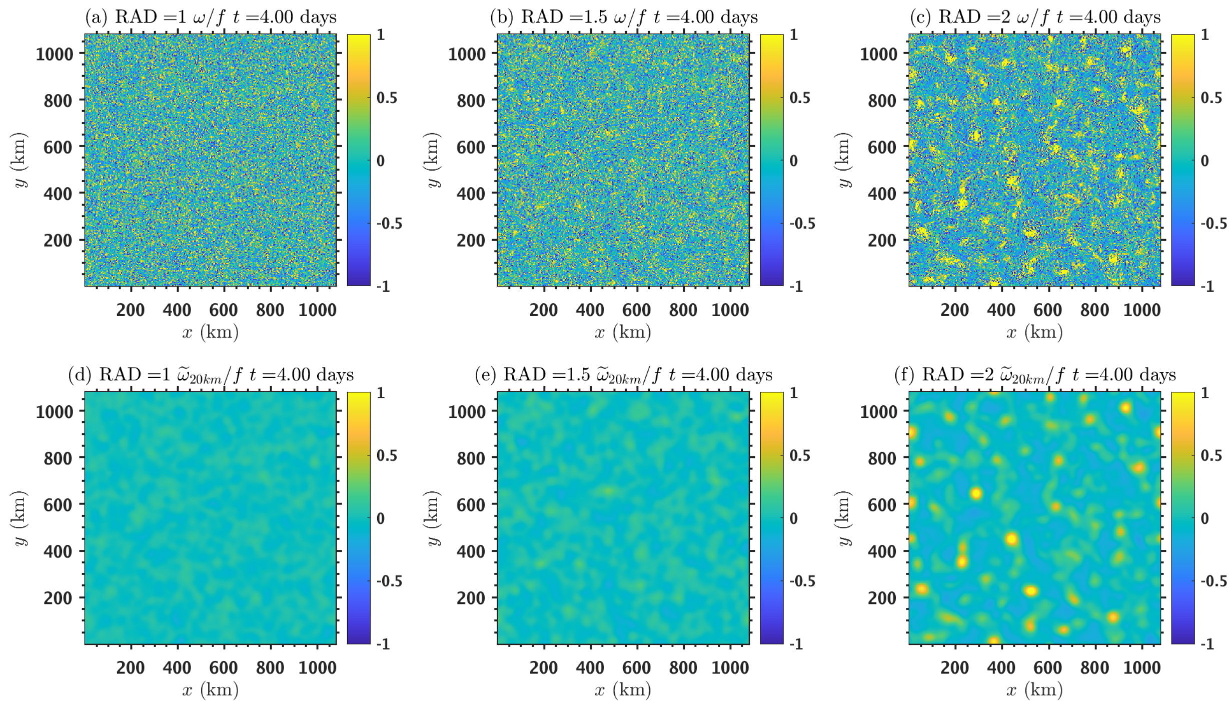

FIG. 9. Some snapshots at $t = 4$ days for Group 2 (changing the longwave radiative feedback strength). The first row is the $z = 5.25$ km (midlevel) relative vertical vorticity normalized by f for (a) the RAD = 1.0 test, (b) the RAD = 1.5 test, (c) the RAD = 2.0 test. The second row is the 20 km filtered field of the first row.

vortex size. Because a typical anvil radius is ~ 10 km (Fig. 10c and f), this indirectly indicates that the early-stage vortex should be sensitive to the anvil size. In addition, the Group 4 experiments demonstrate a robust method of manually controlling the size of mesoscale convective vortices in RRCE, which might be useful for experiments with other purposes.

The experimental results of Groups 3 and 4 confirm the importance of "microscopic" diffusive factors in controlling the vortex length scale. This suggests that the frequently used precipitation-vapor relationship (Sobel et al. 2001; Bretherton et al. 2004; Raymond et al. 2007) should be modified to a nonlocal one. The precipitation (diabatic heating) should depend on a spatially filtered moisture field to account for the spread of convective activity by cold pools and the nonlocal radiative heating by anvil clouds.

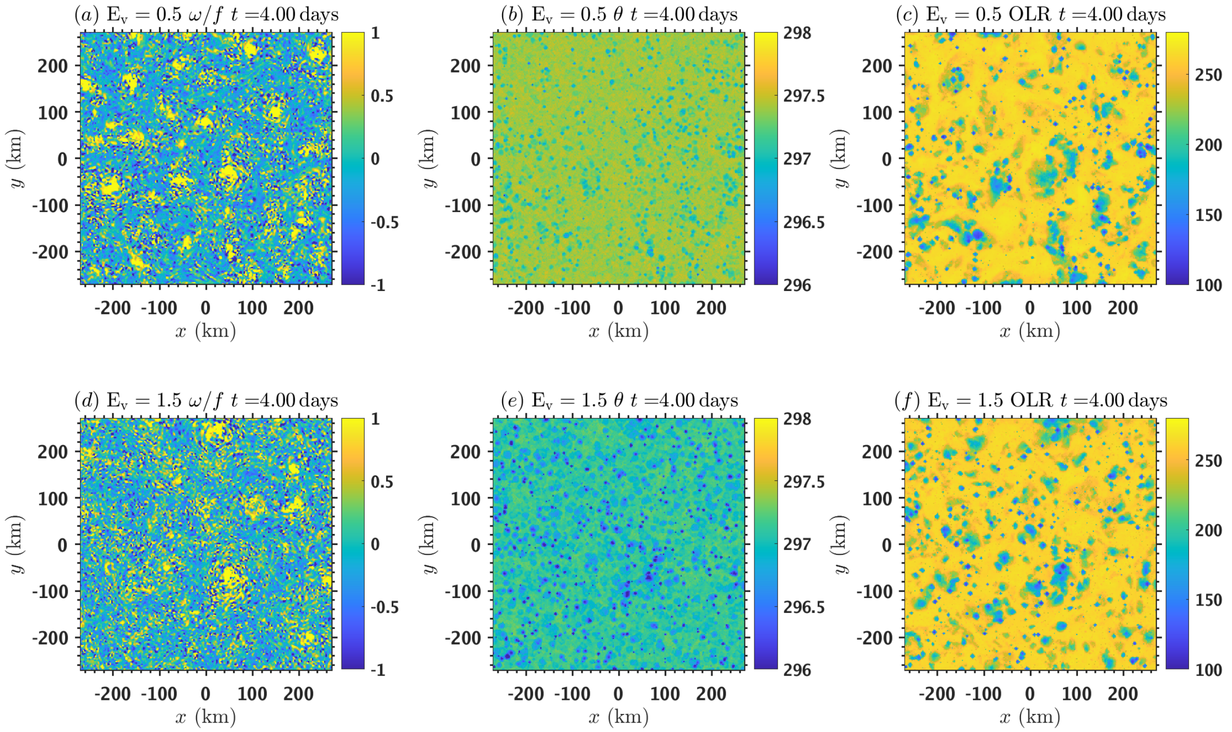

FIG. 10. Some zoom-in snapshots at $t = 4$ days for Group 3 (changing sub-cloud rain evaporation). (a) The $z = 5.25$ km (midlevel) relative vertical vorticity normalized by f for the $\mathrm{E_v} = 0.5$ test. (b) The $z = 25$ m (near surface) potential temperature (unit: K) for the $\mathrm{E_v} = 0.5$ test. The low potential temperature regions correspond to cold pools. (c) The outgoing longwave radiation (OLR, unit: W m^{-2}) for the $\mathrm{E_v} = 0.5$ test. A lower OLR corresponds to a higher longwave emission level and therefore the cloud top height. The quasi-uniform high OLR region is the clear sky region. (d)-(f) are the same as (a)-(c), but for the $\mathrm{E_v} = 1.5$ test.

4. Theory

a. The basic idea

A key challenge for the small-amplitude dynamics of spontaneous tropical cyclogenesis is how to disentangle the mesoscale perturbation and the noisy deep convection. We propose to theoretically study the collective behavior of clouds with *Fourier analysis*.

On the one hand, the clouds are viewed as independent convergence events that produce a wide spectrum of noise in the wavenumber space. This stage has received very little attention, but it is essential because it determines the magnitude of the initial perturbation for the subsequent

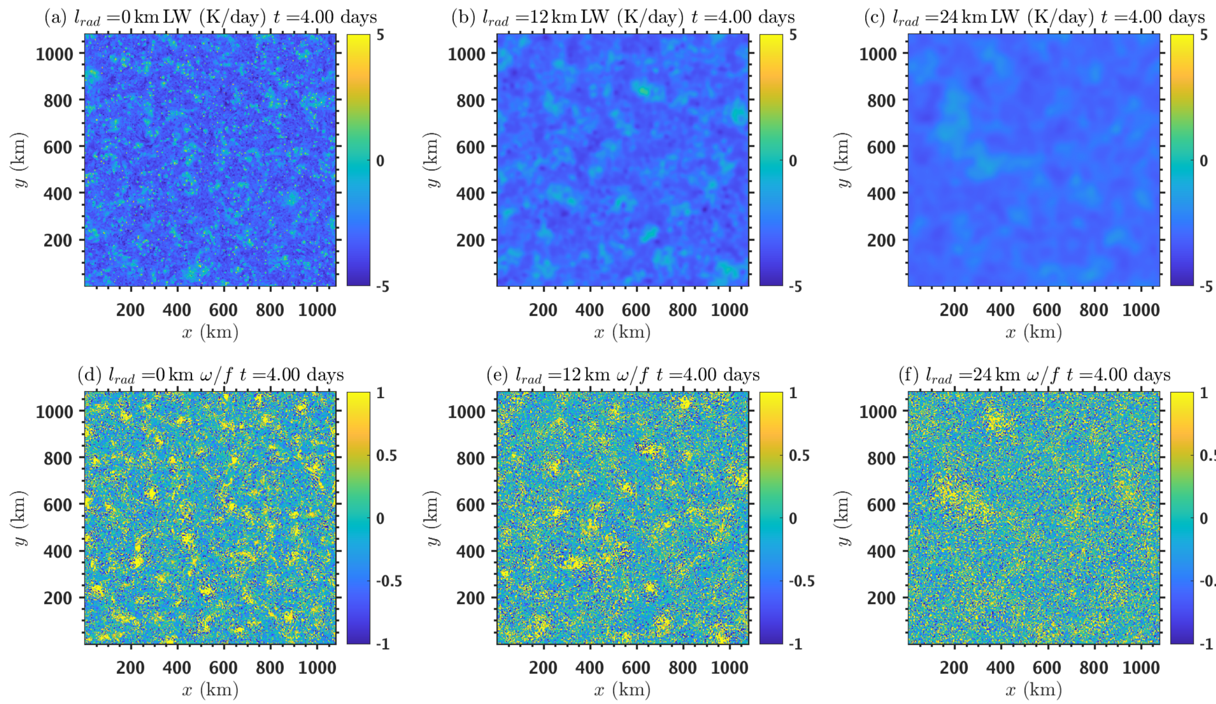

FIG. 11. Some snapshots at $t = 4$ days for Group 4 (filtering the longwave heating rate). The first row is the full longwave heating rate (unit: K day^{-1}, not the horizontal anomaly) at $z = 5.25$ km (midlevel) for (a) the $l_{rad} = 0$ km test, (b) the $l_{rad} = 12$ km test, (c) the $l_{rad} = 24$ km test. The second row is the $z = 5.25$ km (midlevel) relative vertical vorticity normalized by f for (d) the $l_{rad} = 0$ km test, (e) the $l_{rad} = 12$ km test, (f) the $l_{rad} = 24$ km test.

mesoscale instability in the RRCE setup. For the real atmosphere, which is full of disturbance of various origins, the cloud-generated vorticity noise sets the minimum perturbation level.

On the other hand, the clouds can interact with each other. The convective activity can spread via cold pools and anvil clouds' nonlocal longwave radiative heating, which may serve as a mesoscale diffusion. The spread of convective activity spans a mesoscale patch in which the convective strength is smooth and provides a high-wavenumber cutoff for the instability, as is discussed below. The mesoscale component of the cloud-generated noise amplifies with the mesoscale instability, linking the spin-up stage with the exponential growth stage.

For the reference test, the vorticity spectrum for the total horizontal wavenumber K is quite different at the spin-up stage (day 0-2) and the exponential growth stage (day 2-4) (Fig. 12a and b). Before day 2, the vorticity spectrum has a similar shape, and only the magnitude grows. The

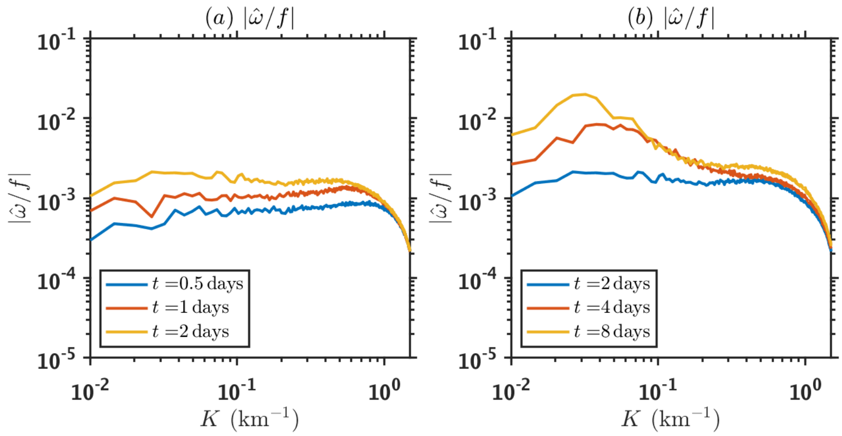

FIG. 12. (a) The midlevel ($z \approx 5.25$ km) vorticity spectrum of the reference test at day 0.5 (blue line), day 1 (red line), and day 2 (orange line). The spectrum is defined as the modulus of the normalized vorticity spectrum $|\hat{\omega}(K)|/f$ (unitless) azimuthally averaged over the total wavenumber $K = (k_x^2 + k_y^2)^{1/2}$, where k_x and k_y are wavenumbers in x and y direction that are defined as 2π over the corresponding wavelength. See (6) and (7) for the expression of Fourier transform. (b) is the same as (a), but for the vorticity spectrum at day 2 (blue line), day 4 (red line), and day 8 (orange line).

spectral shape is close to that of a “red" spectrum, which is relatively uniform above the length scale of a cloud ($K = 0.7$ km^{-1} or 9 km wavelength), in agreement with the hypothesis of Mapes (1997). This spectrum has contributions from two parts: the vorticity monopoles produced by stretching, whose amplitude is uniform for scales above the cloud scale, and the vorticity dipoles produced by tilting, which has a peak near the cloud scale (Vallis et al. 1997). At day 4, a mesoscale spectral peak appears at $K \approx 0.04$ km^{-1} (a wavelength of around 150 km), which roughly corresponds to the vortex spacing in Fig. 3a. The system enters the finite-amplitude stage after day 4. The drop of peak wavenumber corresponds to the growth of vortex size (e.g., due to merger).

The dynamics at the spin-up stage and the exponential growth stage are studied in section 4b and section 4c respectively.

b. The stochastic spin up stage

We start by considering the spin-up of midlevel vorticity between day 0 and day 2. At the early stage, convection occurs randomly and homogeneously in the domain. We study the wavenumber spectrum produced by the random intermittent convective events and use it to explain the vorticity spectrum produced by convection (Fig. 12a), as well as the $R^{1/2}$ behavior of the mesoscale vorticity standard deviation std$(\widetilde{\omega_{20km}})$ at the spin-up stage (Fig. 7).

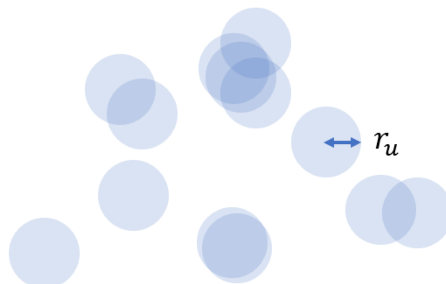

FIG. 13. A schematic diagram of the vorticity growth by convective random stretching. The blue disks denote the relative vorticity produced by the convective events. The radius of each cloud is r_u.

We view the vorticity production at the spin-up stage as the random stretching of planetary vorticity by intermittent convective events, as illustrated in Fig. 13. This treatment is based on three assumptions:

- This model neglects the dipole produced by vorticity tilting, which has little imprint on the mesoscale due to the cancellation between contributions from cloud-scale positive and negative vorticity.
- The model neglects the stretching and advection of relative vorticity, using a small-amplitude assumption.
- This model neglects the negative vorticity produced by radiation-driven large-scale descent because, at the early stage, its magnitude is much weaker than the positive vorticity patches.

Furthermore, we assume each convective cloud to have a fixed radius of r_u (unit: m) and induce an accumulated thickness loss of $-\Delta h$ (unit: m, $\Delta h < 0$) within the convergent layer. The midlevel vorticity increment produced by a convective event is $\Delta\omega$:

$$\Delta\omega \approx -f\frac{\Delta h}{H}, \tag{3}$$

where H (unit: m) is the depth of the convergent layer (around 5000 m according to the vertical velocity profile in Fig. 4b). The vorticity field produced by the random superposition of an N_u number of Gaussian-shape vorticity increments is denoted as ω_n (unit: s^{-1}):

$$\omega_n = \Delta\omega \exp\left[-\frac{(x-x_n)^2+(y-y_n)^2}{r_u^2}\right], \quad n = 1,\ 2,\ ...,N_u, \tag{4}$$

where (x_n, y_n) is the central position of the n^{th} convective event. Because each convection is assumed identical, the accumulated rainfall R is proportional to the number of convective events N_u:

$$R \propto N_u. \tag{5}$$

Next, we use the wavenumber spectrum of vorticity to quantitatively link the random superposition process with std$(\widetilde{\omega_{20km}})$. In studying 2D turbulence, Benzi et al. (1992) derived the vorticity spectrum produced by a large number of round vortices of different sizes at random locations. When the vortex size is set to be identical, their solution shows that the shape of the superposed spectrum is the same as that of an individual vortex, in agreement with our diagnosed spectrum before day 2 (Fig. 12a). However, because their focus is the shape rather than the magnitude of the spectrum, they did not further calculate how the magnitude depends on the convective seeding number N_u, which is key to our time-dependent problem. The finite-domain Fourier transform of ω_n is denoted as $\hat{\omega}_n$ (unit: s^{-1}):

$$\begin{aligned}\hat{\omega}_n &\equiv \frac{1}{L^2}\int_{-L/2}^{L/2}\int_{-L/2}^{L/2} \omega_n \exp\left[-i(k_x x + k_y y)\right] dxdy \\ &\approx \frac{1}{L^2}\int_{-\infty}^{\infty}\int_{-\infty}^{\infty} \omega_n \exp\left[-i(k_x x + k_y y)\right] dxdy \\ &= \lambda\Delta\omega\frac{r_u^2}{4\pi}\exp\left[-\frac{r_u^2(k_x^2+k_y^2)}{4}\right]\underbrace{\exp\left[i(k_x x_n + k_y y_n)\right]}_{\text{random shift factor}},\end{aligned} \tag{6}$$

for wavenumbers:

$$k_x = \frac{2\pi}{L}m_x,\ k_y = \frac{2\pi}{L}m_y, \quad m_x,\ m_y \in \mathbb{Z}. \tag{7}$$

Here L (unit: m) is the domain width. In (6), we have used the infinite-domain Fourier transform of the Gaussian function to approximate the finite-domain transform, which is valid due to $r_u \ll L$. The parameter $\lambda = 4\pi^2/L^2$ (unit: m^{-2}) in (6) is a conversion coefficient.

The modulus of the wavenumber spectrum of the randomly superposed field $\omega = \sum_{n=1}^{N_u} \omega_n(x, y)$, $|\hat{\omega}|$, has a similar shape with the individual one $|\hat{\omega}_n|$, as has been reported by Benzi et al. (1992):

$$
\begin{aligned}
|\hat{\omega}| &= \left|\sum_{n=1}^{N_u} \hat{\omega}_n\right| \\
&= \lambda \Delta\omega \frac{r_u^2}{4\pi} \exp\left[-\frac{r_u^2(k_x^2 + k_y^2)}{4}\right] \left|\sum_{n=1}^{N_u} \exp\left[i(k_x x_n + k_y y_n)\right]\right| \\
&\approx \underbrace{\lambda \Delta\omega \frac{r_u^2}{4\pi} \exp\left[-\frac{r_u^2(k_x^2 + k_y^2)}{4}\right]}_{|\hat{\omega}_n|} N_u^{1/2}.
\end{aligned}
\tag{8}
$$

The modulus of the sum of the random shift factor, which is the amplitude of a group of incoherent waves, is $N_u^{1/2}$. Finally, we substitute (8) into Parseval's theorem to explain why $\mathrm{std}(\widetilde{\omega_{20km}}) \propto R^{1/2}$ in Fig. 7. Note that $\mathrm{std}(\widetilde{\omega_{20km}})$ is the standard deviation of the *mesoscale* vorticity. We let l (unit: m) be an arbitrary length scale above the cloud scale r_u. Using (8), we get:

$$
\begin{aligned}
\mathrm{std}(\widetilde{\omega_l}) &\approx \left[\frac{L^2}{4\pi}\int_0^\infty |\hat{\omega}|^2 \exp\left(-\frac{K^2 l^2}{2}\right) 2\pi K dK\right]^{1/2} \\
&= \left[\frac{L^2}{4\pi}\int_0^\infty |\hat{\omega}_n|^2 N_u \exp\left(-\frac{K^2 l^2}{2}\right) 2\pi K dK\right]^{1/2} \\
&= N_u^{1/2} \mathrm{std}(\widetilde{\omega_n}) \\
&\propto R^{1/2}.
\end{aligned}
\tag{9}
$$

Equation (9) indicates that the standard deviation of $\widetilde{\omega_l}$ is $N_u^{1/2}$ times the standard deviation of the filtered vorticity of a single convectively generated vorticity patch. This $N_u^{1/2}$ scaling applies to any l. Letting $l = 20$ km, (9) turns out to be $\mathrm{std}(\widetilde{\omega_{20km}}) \propto R^{1/2}$.

Because our theory considers vortex stretching to be the only path for generating mesoscale vorticity, the pattern of absolute vorticity originates from the aggregation of planetary vorticity. The theory predicts $\mathrm{std}(\widetilde{\omega_{20km}}) \propto f$, which generally agrees with the Group 1 experiments (Fig.

7e). The slightly larger std($\widetilde{\omega_{20km}}$)$/f$ for a smaller f might be due to the relatively small imprint of dipoles on the mesoscale, whose relative vorticity is independent of f.

c. The mesoscale instability

1) Diagnosing the growth rate

In this subsection, we study how the mesoscale vorticity perturbation produced at the spin-up stage amplifies with the mesoscale instability at the exponential growth stage. The first row of Fig. 14 shows the spectral growth rate σ (unit: s^{-1}) between day 2.5 and day 3.5 of all the experiments. To smear out the noise, we use a moving time average:

$$\sigma(K,t) = \frac{1}{13}\sum_{i=-6}^{6}\sigma_i(K,t), \quad \sigma_i(K,t) = \frac{\ln\left[|\hat{\omega}(K, 3.5\,\mathrm{days} + i\Delta t)|/|\hat{\omega}(K, 2.5\,\mathrm{days} + i\Delta t)|\right]}{1\ \mathrm{day}}, \tag{10}$$

where $K = (k_x^2 + k_y^2)^{1/2}$ is the total horizontal wavenumber, and the spectrum $\hat{\omega}$ has been averaged azimuthally. Here we let Δt = 1 hour and use 13 sampled points around both day 2.5 and day 3.5. The growth rate calculated with 1, 3, 5, 7, and 9 sampling points are shown in Fig. S1-S5, which show no qualitative difference. There is a most unstable wavenumber in each experiment. [5] We will derive an analytical expression of the spectral growth rate.

2) The governing equation

We start from the small-amplitude hydrostatic Boussinesq equation system, which ignores the change of density with height in the mass continuity:

$$\frac{\partial u}{\partial t} - fv = -\frac{\partial \phi'}{\partial x} - \frac{u}{\tau_d}, \tag{11}$$

$$\frac{\partial v}{\partial t} + fu = -\frac{\partial \phi'}{\partial y} - \frac{v}{\tau_d}, \tag{12}$$

$$0 = -\frac{\partial \phi'}{\partial z} + b, \tag{13}$$

[5]For the reference test, there is a second growth rate peak at $2\pi/K \approx 700$ km. We consider this a spurious event because as the scale approaches the domain size, there are few wavenumber points for calculating the azimuthal average in the wavenumber space. In addition, there is no such second peak in another experiment with the same parameter setting but a different set of initial noise, as is shown in Fig. S6. Similarly, the second peak of the RAD = 1.5 test at $2\pi/K \approx 700$ km disappears when a different sampling number is used (see Fig. S1-S5), so we do not consider it as a physically meaningful feature.

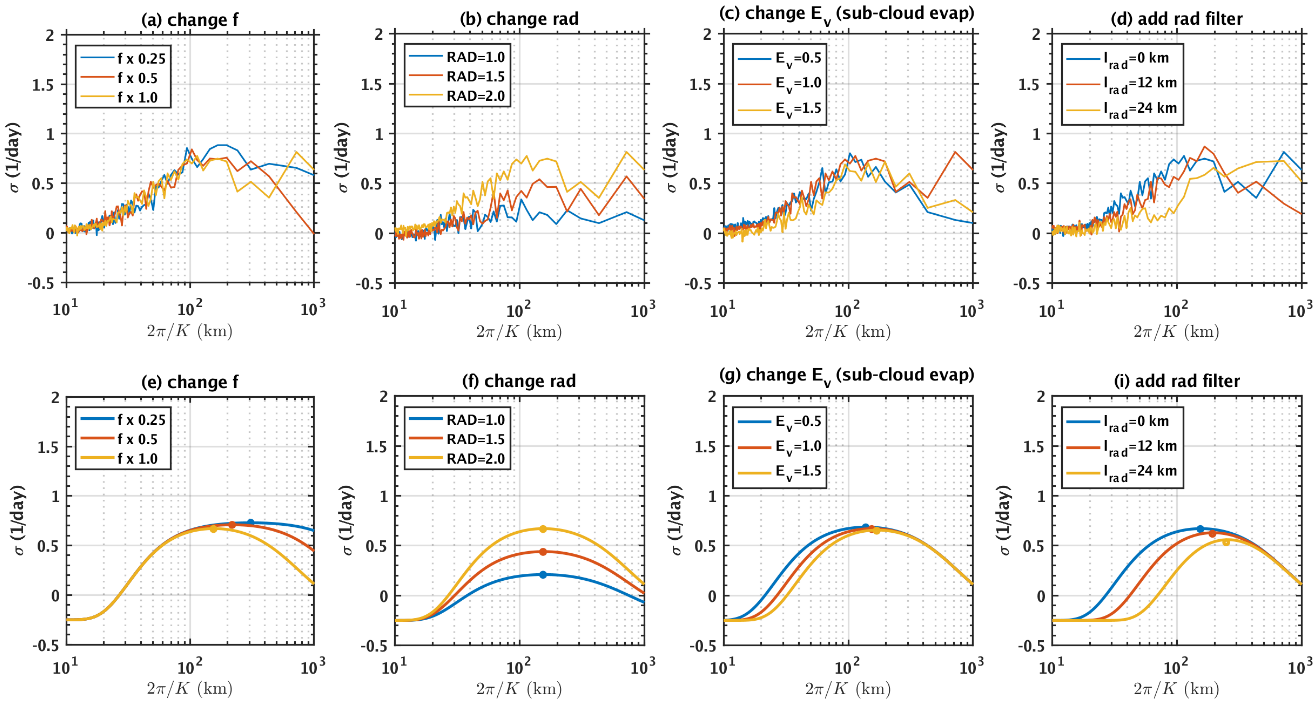

FIG. 14. The upper row shows the spectral growth rate of of all the simulations between day 2.5 and day 3.5 calculated with (10). (a) vary the Coriolis parameter, with $f = 0.25\times10^{-4}$ s^{-1} (the blue line), $f = 0.5\times10^{-4}$ s^{-1} (the red line), and $f = 10^{-4}$ s^{-1} (the orange line). (b) vary the horizontal anomaly of longwave radiative heating, with RAD = 1.0 (the blue line), RAD = 1.5 (the red line), and RAD = 2.0 (the orange line). (c) vary the sub-cloud rain evaporation rate, with E_v = 0.5 (the blue line), E_v = 1.0 (the red line), and E_v = 1.5 (the orange line). (d) vary the Gaussian filter on the horizontal anomaly of longwave radiative heating, with $l_{rad} = 0$ km (no filter, the blue line), l_{rad} = 12 km (the red line), and l_{rad} = 24 km (the orange line). The lower row shows the theoretical spectral growth rate (26), with the same line color as in the upper row. The corresponding dots denote the most unstable wavelength $2\pi/K_m \approx (\pi/\sqrt{2})(L_cL_R)^{1/2}$ and its growth rate $\sigma_m \approx (1/\tau)(1-L_c/L_R)-1/\tau_d$ shown in (28) and (29) respectively.

$$\frac{\partial u}{\partial x}+\frac{\partial v}{\partial y}+\frac{\partial w}{\partial z}=0, \tag{14}$$

$$\frac{\partial b}{\partial t}=-N^2w+\underbrace{\beta(1+\epsilon_{rad})N^2\widetilde{w_{L_c}}+\alpha(1+\epsilon_{rad})\widetilde{q'_{L_c}}}_{\text{diabatic heating}}-\frac{b}{\tau_d}, \tag{15}$$

$$\frac{\partial q'}{\partial t} = \gamma w - \frac{q'}{\tau_d}. \tag{16}$$

Here u, v, and w denote the three components of momentum in the Cartesian coordinate, ϕ' denotes the horizontal anomaly of geopotential (unit: m^2 s^{-2}), b denotes buoyancy (unit: m s^{-2}), and q' denotes the horizontal anomaly of free-tropospheric water vapor mixing ratio. The parameter $N \approx 10^{-2}$ s^{-1} is the buoyancy frequency. The parameter γ (unit: m^{-1}) denotes the vertical gradient of the horizontally averaged water vapor mixing ratio, with a minus sign. A positive γ means a mesoscale updraft moistens the atmosphere. The τ_d is the time scale of damping, which is assumed to be identical for u, v, b, and q'.[6]

The diabatic heating term in (15) has two parts: the wave-CISK-radiation feedback and the moisture-radiation feedback. The cloud longwave radiative feedback serves as an amplification factor ($\epsilon_{rad} \approx 0.9$ for the reference test), and the convective spreading serves as a filter.

- The $\beta N^2(1+\epsilon_{rad})\widetilde{w_{L_c}}$ is the wave-CISK-radiation part. It denotes the component of diabatic heating that depends (quasi-)instantaneously on the mesoscale vertical advection and its amplification by the cloud longwave radiative feedback. The $\widetilde{w_{L_c}}$ is the vertical velocity smoothed by an L_c-scale Gaussian filter. The L_c is a bulk convective smoothing length that consists of a natural component and an artificial component:

$$L_c = (\underbrace{l_c^2}_{\text{natural}} + \underbrace{l_{rad}^2}_{\text{artificial}})^{1/2}. \tag{17}$$

Here l_c is the natural convective spreading length scale that represents the spread of convective activity by cold pools and the nonlocal radiative effect of anvil clouds (and gravity waves, vapor lateral mixing, etc.), and l_{rad} is the artificial radiative heating filter that is only nonzero in the Group 4 experiments. We leave the separation of the cold pool effect and the nonlocal radiative effect on l_c for future works. The β is the magnitude ratio of the component of latent heating associated with $\widetilde{w_{L_c}}$ to adiabatic cooling, which is suggested to be smaller than but close to unity for the first baroclinic mode by Haertel and Kiladis (2004). The β reduces the

[6]For u and v, the τ_d denotes the vertical momentum transport by deep convection, which is estimated to be on the order of 10 days for the first baroclinic mode (Romps 2014). For b, the τ_d denotes Newtonian radiative cooling, whose order might be a day or longer (Wu et al. 2000). For q', the τ_d denotes the elimination of free-tropospheric water vapor anomaly by precipitation, which is prescribed order of 1 day in some tropical wave models but remains physically uncertain (Fuchs and Raymond 2002).

gravity wave speed. When $\beta(1+\epsilon_{rad}) > 1$, the effective stratification is unstable, leading to the wave-CISK instability (Dunkerton and Crum 1991).

- The $\alpha(1+\epsilon_{rad})\widetilde{q'_{L_c}}$ is the moisture-radiation part. It denotes convective enhancement by free tropospheric moisture and its amplification by the cloud longwave radiative feedback. The parameter α (unit: m s^{-3}) measures the sensitivity of convection to free-tropospheric vapor content (Bretherton et al. 2004; Raymond et al. 2007). The information from the previous mesoscale vertical motion is stored in q'. Here $\widetilde{q'_{L_c}}$ denotes the q' smoothed by a Gaussian filter of length L_c that represents the convective spreading.

In the appendix, we consider the $\beta(1+\epsilon_{rad}) > 1$ case (wave-CISK-radiation instability) with convective spreading and derive its spectral growth rate. We show that the most unstable mode's growth rate of the wave-CISK-radiation instability has a strong sensitivity to f, which disagrees with our Group 1 experiments (changing f) where the sensitivity to f is weak. This indicates that our experiments do not lie in the regime of the wave-CISK-radiation instability. Thus, the instability is controlled by moisture-radiation feedback. However, the wave-CISK-radiation feedback could modulate the instability by slowing down the convectively coupled gravity wave.

3) Solving the growth rate

Now we are ready to perform the linear stability analysis. As for the vertical structure of the perturbation, the system can be described with the superposition of the first and second baroclinic modes. The first baroclinic mode represents the convective heating by deep convection, and the second baroclinic mode represents the stratiform heating which is negative at the lower level due to the strong rain evaporation there (Mapes 2000; Liu and Moncrieff 2004). For simplicity, we start by considering only the first baroclinic mode with the tropospheric depth $H_T \approx 12$ km as the depth scale, which grasps the essential feature of the spectral growth rate. The vertical structure of all the variables is assumed to be sinusoidal:

$$\begin{gathered}u = U\cos\left(\frac{\pi}{H_T}z\right), \quad v = V\cos\left(\frac{\pi}{H_T}z\right), \quad w = W\sin\left(\frac{\pi}{H_T}z\right), \\ \phi' = \Phi\cos\left(\frac{\pi}{H_T}z\right), \quad b = B\sin\left(\frac{\pi}{H_T}z\right), \quad q' = Q\sin\left(\frac{\pi}{H_T}z\right).\end{gathered} \tag{18}$$

We further consider a set of horizontal normal modes that grow exponentially:

$$(U, V, W, \Phi, B, Q) = \left(\check{U}, \check{V}, \check{W}, \check{\Phi}, \check{B}, \check{Q}\right) e^{i(k_x x + k_y y)} e^{\sigma t}, \tag{19}$$

where k_x and k_y are the components of the horizontal wavenumber. Substituting (18) and (19) into (11)-(16), and rewriting the momentum equations as the vorticity equation and the divergence equation, we get:

$$\sigma \check{\omega} = -f \check{\delta} - \frac{\check{\omega}}{\tau_d}, \tag{20}$$

$$\sigma \check{\delta} = K^2 \check{\Phi} + f \check{\omega} - \frac{\check{\delta}}{\tau_d}, \tag{21}$$

$$\sigma \check{\Phi} + c_e^2 \check{\delta} = -\frac{H_T}{\pi} \alpha (1 + \epsilon_{rad}) \check{Q} e^{-\frac{K^2 L_c^2}{4}} - \frac{\check{\Phi}}{\tau_d}, \tag{22}$$

$$\sigma \check{Q} = -\frac{H_T}{\pi} \gamma \check{\delta} - \frac{\check{Q}}{\tau_d}. \tag{23}$$

Here $\check{\omega} \equiv i k_x \check{V} - i k_y \check{U}$ and $\check{\delta} \equiv i k_x \check{U} + i k_y \check{V}$ denote the normal mode form of vorticity and divergence. The parameter c_e is the effective speed of the convectively coupled internal gravity wave that is smaller than the dry gravity wave speed c when the wavelength is significantly larger than L_c:

$$c_e = \left[1 - \beta(1 + \epsilon_{rad}) e^{-\frac{K^2 L_c^2}{4}}\right]^{1/2} \underbrace{\frac{N H_T}{\pi}}_{c} \approx \left[1 - \beta(1 + \epsilon_{rad}) e^{-\frac{K^2 L_c^2}{4}}\right]^{1/2} \times 40 \text{ m s}^{-1}, \tag{24}$$

where we have used $N \approx 10^{-2}$ s^{-1}, and $H_T \approx 12$ km to get $c = N H_T / \pi \approx 40$ m s^{-1}.

Equations (20)-(23) render an eigenvalue problem with respect to the growth rate σ, which yields:

$$\frac{\left(\sigma + \frac{1}{\tau_d}\right)^2}{K^2 c_e^2} \left[1 + \frac{f^2}{\left(\sigma + \frac{1}{\tau_d}\right)^2}\right] = \frac{\alpha \gamma (1 + \epsilon_{rad})}{\left(\sigma + \frac{1}{\tau_d}\right) c_e^2} \frac{H_T^2}{\pi^2} e^{-\frac{K^2 L_c^2}{4}} - 1. \tag{25}$$

The left-hand-side of this expression can be approximated as $f^2/(K^2 c_e^2)$ by assuming $\sigma + \frac{1}{\tau_d} \ll f$, which is a quasi-geostrophic (QG) approximation that filters out the transient component of gravity waves. The diagnosed growth rate in Fig. 14 shows that the $\sigma + \frac{1}{\tau_d} \ll f$ condition is marginally satisfied for the $f = 0.25 \times 10^{-4}$ s^{-1} test in Group 1 and well-satisfied for other tests. We get a simplified expression of σ:

$$\sigma+\frac{1}{\tau_d}\ll f: \quad \sigma\approx\frac{1}{\tau}\left(\frac{1}{K^2L_R^2}+1\right)^{-1}e^{-\frac{K^2L_c^2}{4}}-\frac{1}{\tau_d}, \tag{26}$$

where $L_R=c_e/f$ is the effective Rossby deformation radius, and τ is the reference growth time scale due to the moisture-radiation feedback:

$$\tau=\frac{c_e^2}{\alpha\gamma(1+\epsilon_{rad})}\frac{\pi^2}{H_T^2}=\frac{N^2}{\alpha\gamma}\frac{1-\beta(1+\epsilon_{rad})e^{-\frac{K^2L_c^2}{4}}}{1+\epsilon_{rad}}. \tag{27}$$

We make three remarks on (26) and (27):

- The reference growth rate $1/\tau$ is higher for a higher ϵ_{rad} due to two factors: the direct contribution of radiative heating to the diabatic heating and the reduction of the effective gravity wave speed c_e.

- The reference growth rate $1/\tau$ is a function of K. The longer the wavelength, the slower the wave speed and, therefore, the higher $1/\tau$ is.

- The $1/\tau-1/\tau_d$ is an upper bound of the spectral growth rate. Thus, a necessary condition for satisfying the $\sigma+\frac{1}{\tau_d}\ll f$ condition in (26) is $f\tau\gg 1$. When $1/\tau-1/\tau_d>0$, the system has a negative effective gross moist stability.

4) Comparison with simulations

The four quantities τ_d, τ, L_R, L_c control the theoretical spectral growth rate (26). Note that τ and L_R are functions of K. We lack carefully benchmarked theories for any four quantities, with l_{rad} the only controllable component that influences L_c. Thus, we prescribe the four quantities to make them fit the diagnosed growth rate and leave their theoretical determination for future work. The value of our theoretical spectral growth rate lies in its basic shape.

Furthermore, we assume $KL_c\to 0$ in the expression of L_R and τ to make them constant. This simplification is based on a scale separation assumption between convective spreading and the effective Rossby deformation radius: $L_c\ll L_R$, which will be shown to fit the spectral growth rate.

- We let $KL_c \to 0$ in L_R because a wave with a higher K is less coupled to convection and has a larger L_R, increasing the scale separation between the wavelength and the deformation radius. The deformation radius cannot significantly influence the wave propagation when $KL_R \gg 1$, so we ignore the influence of K on L_R.[7]

- We let $KL_c \to 0$ in τ because a higher K has a higher effective gravity wave speed c_e and a smaller $1/\tau$. Meanwhile, the $e^{-\frac{K^2 L_c^2}{4}}$ factor of the moisture-radiation feedback damps the high K mode. The two effects have the same trend, so the dependence of τ on K does not change the basic shape of the spectral growth rate. Thus, we ignore the dependence of τ on K for simplicity.

For the reference test, we use $\tau_p^{-1} = 0.25$ day^{-1}, $\tau^{-1} = 1$ day^{-1}, $L_R = 120$ km (using $c_e = 12$ m s^{-1}), and $L_c = 10$ km.

- For Group 1, we use $L_R = 480$ km ($f = 0.25 \times 10^{-4}$ s^{-1}), $L_R = 240$ km ($f = 0.5 \times 10^{-4}$ s^{-1}), and $L_R = 120$ km ($f = 1.0 \times 10^{-4}$ s^{-1}), with all other parameters fixed.

- For Group 2, we use $\tau^{-1} = 0.5$ day^{-1}, 0.75 day^{-1}, and 1 day^{-1}. This setting assumes τ^{-1} increases linearly with RAD. An additional RAD = 0.5 test (not shown) is close to the neutral mode, which is also evident from an extrapolation of the diagnosed growth rate in Fig. 14b. Thus, we let RAD = 0.5 obey $1/\tau = 1/\tau_d = 0.25$ day^{-1}, which is the basis of how we choose τ_d.[8] As for the most unstable wavelength, the theory predicts a higher RAD reduces c_e and therefore L_R and the most unstable wavelength. This is not obvious in the diagnosed growth rate (Fig. 14b). Thus, we use the reference $L_R = 120$ km in calculating the theoretical spectral growth rate of Group 2.

- For Group 3, we use $L_c = l_c = 8$ km, 10 km, and 12 km, which has the same order of magnitude as the deep convective cloud spacing (e.g. Nissen and Haerter 2021; Fu and O'Neill 2022). We are unaware of any model for the spread of convective activity by cold pools. However, there is a semi-empirical theory by Yang (2020) for the spread of convective activity by gravity waves, which might share some analogies to cold pool.

- For Group 4, we use $L_c = \left[(10\text{ km})^2 + l_{rad}^2\right]^{1/2} = 10$ km, 15.6 km, and 26 km.

---

[7] This physical argument appears mathematically as the $1/(K^2 L_R^2)$ term in (26), which is much smaller than unity when $KL_R \gg 1$. Thus, σ is insensitive to L_R at a high K range.

[8] Based on the simple radiative model of Wing and Emanuel (2014) and Emanuel et al. (2014), Windmiller and Craig (2019) considered the influence of vapor on the emissivity and obtained $\tau^{-1} \approx 0.5$ day^{-1}, which has the same order of magnitude as the τ^{-1} used for our RAD = 1.0 test.

Table 2 summarizes the parameters for calculating the theoretical growth rate. The second row of Fig. 14 shows the theoretical spectral growth rate calculated with (26) generally agrees with the simulations. The main difference is at the high-K range where the σ is negative in theory but near zero in the simulations. This is because convection keeps producing vorticity anomaly at the small scale and balances the damping. This factor only needs to be considered in the mesoscale instability model if the upscale growth of the small-scale perturbations is essential, which is still unknown.

TABLE 2. The parameters for calculating the theoretical spectral growth rate.

Name	τ_d^{-1} (day^{-1})	τ^{-1} (day^{-1})	L_R (km)	L_c (km)
Reference	0.25	1	120	10
Group 1-A	0.25	1	480	10
Group 1-B	0.25	1	240	10
Group 2-A	0.25	0.5	120	10
Group 2-B	0.25	0.75	120	10
Group 3-A	0.25	1	120	8
Group 3-B	0.25	1	120	12
Group 4-A	0.25	1	120	15.6
Group 4-B	0.25	1	120	26

5) The most unstable wavelength

Next, we study the most unstable wavelength, the early-stage mesoscale vortex's characteristic length scale. The most unstable wavenumber K_m is obtained by letting $\partial\sigma/\partial K = 0$ in (26):

$$K_m \approx \left(\frac{2}{L_c L_R} - \frac{1}{2L_R^2}\right)^{1/2} \approx \left(\frac{2}{L_c L_R}\right)^{1/2}, \tag{28}$$

which states that *the most unstable wavelength of a small-amplitude tropical convective vortex is proportional to the geometric average of L_R and L_c.*[9] In deriving (28), we have assumed a scale separation between the convective spreading and the effective deformation radius: $L_c/L_R \ll 1$, which is valid unless f is large enough ($\gtrsim 2\times10^{-4}$ s^{-1} based on our numerical simulation experience) to influence the cloud dynamics. For the reference test, L_c = 10 km and L_R = 120

[9]In comparison, the most unstable wavelength of a small-amplitude midlatitude baroclinic eddy is proportional to L_R (Vallis 2017). This indicates that the Rossby deformation radius still controls the vortex size in the tropics but to a less extent than the midlatitude.

km yield $2\pi/K_m \approx 154$ km. Equation (28) agrees with the spectral growth rate diagnosed from the simulations (Fig. 14) that a larger E_v (sub-cloud rain evaporation), or a larger l_{rad} (radiative smoothing length) increases the vortex size. The theory predicts that K_m is higher for a higher RAD or a higher f where L_R is smaller, but this is unclear from the diagnosed growth rate. We make two remarks:

- In agreement with the traditional Ekman-CISK model, the most unstable wavelength decreases with decreasing L_R because a larger Coriolis parameter makes L_R smaller and makes the compensation descent of a convective vortex more concentrated. The adiabatic heating associated with the compensation descent diminishes the updraft buoyancy and disfavors the instability (Bjerknes 1938; Emanuel et al. 1994). Thus, the most unstable wavelength must shift to a smaller value to make the system less suppressed by the Coriolis force.
- The K_m is very sensitive to L_c despite its small magnitude. This indicates that the cloud dynamics, which is strongly modulated by microphysics (e.g., sub-cloud rain evaporation and ice sublimation rate), could play an important role in setting the size of an early-stage mesoscale convective vortex.

The growth rate of the most unstable mode σ_m is obtained by substituting (28) into (26):

$$
\begin{aligned}
\sigma_m &= \frac{1}{\tau}\left(1+\frac{1}{K_m^2 L_R^2}\right)^{-1} e^{-\frac{K_m^2 L_c^2}{4}} - \frac{1}{\tau_d} \\
&= \frac{1}{\tau}\left(1+\frac{1}{2}\frac{L_c}{L_R}\right)^{-1} e^{-\frac{1}{2}\frac{L_c}{L_R}} - \frac{1}{\tau_d} \\
&\approx \frac{1}{\tau}\left(1-\frac{L_c}{L_R}\right) - \frac{1}{\tau_d}.
\end{aligned} \tag{29}
$$

In deriving the third line, we have again used the scale separation assumption: $L_c/L_R \ll 1$. The most important factor in determining σ_m is τ and τ_d. The second important one is L_c/L_R: a higher L_c/L_R reduces σ_m. Physically, this is because the convective spreading damps the short-wavelength mode, and the Coriolis force damps the long-wavelength mode. The closer these two scales are, the more significantly they suppress the most unstable mode's growth. Because $L_c/L_R \ll 1$, we conclude that σ_m is insensitive to L_c and L_R, which explains the weak sensitivity of σ_m to f, E_v and l_{rad} in the simulations (Fig. 14).

Despite the importance of the most unstable mode, we should be cautious that it can denote the vortex size *only if* the spectral instability band, which is sandwiched between L_c and L_R, is narrow. As f gets lower, L_R gets larger, and the instability band gets wider, as is the case of our $f = 0.25 \times 10^{-4}$ s^{-1} test (Fig. 14e). Many adjacent modes contribute to the growing perturbation in such a wide-band case. Though there is not a single dominant mode, the shorter-wavelength components are damped more heavily by the convective spreading effect, rendering a coarsening process (e.g., similar to the diffusion term in Windmiller and Craig 2019). For $f \to 0$, the $\sigma \ll f$ assumption for deriving (26) breaks down. Is there any long-wavelength cutoff other than L_R for the instability band in the $f \to 0$ regime? This question motivates us to theoretically explore the $\sigma \gg f$ regime of the moisture-radiation instability, which is beyond our numerical experiments but provides a broader picture of the parameter space.

6) A map for the parameter space

In fact, for $\sigma \gg f$ ($f\tau \ll 1$), which is of interest to tropical cyclogenesis at a low latitude (Carstens and Wing 2020, 2022), there is a long-wavelength cutoff that replaces the role of L_R in the $f\tau \gg 1$ regime. This is because, for $\sigma \gg Kc_e$, the wavelength is so long that the growth signal from the center of the convective region cannot reach its rim within a growth time scale.

For $1/\tau \ll Kc_e$ where the wavelength of interest is relatively short, the growth signal is "well received" within a wavelength, and the system obeys weak temperature gradient approximation (WTG, Sobel et al. 2001). The asymptotic expression of σ at the long- and short-wavelength limits are:

$$f\tau \ll 1: \quad \sigma \approx \begin{cases} \left(\frac{K^2 c_e^2}{\tau}\right)^{1/3} e^{-\frac{K^2 L_c^2}{12}} - \frac{1}{\tau_d}, & \frac{1}{\tau} \gg Kc_e, \\ \frac{1}{\tau} e^{-\frac{K^2 L_c^2}{4}} - \frac{1}{\tau_d}, & \frac{1}{\tau} \ll Kc_e. \end{cases} \tag{30}$$

This long-wavelength cutoff exists in the moisture-radiation instability model of Fuchs and Raymond (2002), but they did not discuss the physical meaning or report the asymptotic expression. The matching scale between these two regimes (named L_τ) can be obtained by equating their growth rate and assuming that L_c is much shorter than this matching scale. This yields an L_τ which serves as the long-wavelength cutoff for $f\tau \ll 1$:

$$L_\tau = \tau c_e. \tag{31}$$

For $\tau \sim 2$ day and $c_e \sim 12$ m s^{-1}, we get $L_\tau \sim 2000$ km. Such a large cutoff length scale might be relevant to the size of a convective self-aggregation patch in a large domain (Patrizio and Randall 2019). A self-aggregated convective patch is the first step towards spontaneous tropical cyclogenesis at a low latitude (Carstens and Wing 2020).

The above findings are summarized in a map for the parameter space of spontaneous tropical cyclogenesis with the moisture-radiation instability ($c_e^2 > 0$), as is shown in Fig. 15. The problem is controlled by two nondimensional parameters: $f\tau$ and $Kc_e\tau$. As $f\tau$ decreases from the $L_R \sim L_c$ point (the upper right corner), the instability band gets wider, and the instability becomes more multiscale.

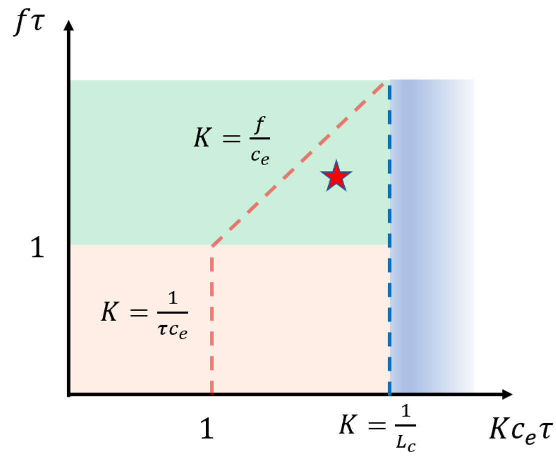

FIG. 15. A sketch of the parameter space for the moisture-radiation instability with the convective spreading effect. The $f\tau$ and $Kc_e\tau$ are two key nondimensional parameters. The dashed red line denotes the long-wavelength cutoff prescribed by L_R and L_τ in the $f\tau > 1$ and $f\tau < 1$ regime, respectively. The dashed blue line denotes the short-wavelength cutoff prescribed by the convective spreading length scale L_c. The red star denotes the approximate location of the most unstable wavelength of our numerical experiments.

5. Conclusion

This paper uses cloud-permitting simulations to study the small-amplitude stage of spontaneous tropical cyclogenesis over a uniform sea surface temperature. The longwave radiative feedback has been found to be vital for the early-stage growth (Wing et al. 2016; Muller and Romps 2018; Yang and Tan 2020; Ruppert et al. 2020), but the growth rate and length scale of the early-stage vortices did not previously have a theoretical basis. In particular, it remains unclear to what extent we can view this process as a linear hydrodynamic instability because it is hard to separate the radiative feedback from the noisy convective-scale dynamics.

To disentangle the noisy background convection and the longwave radiative feedback, we double the horizontal anomaly of longwave radiative heating to enhance the signal. A regular vortex pattern with a wavelength of around 150 km is identified in the midlevel vorticity field on day 4. Using the standard deviation of a smoothed midlevel vorticity ($\mathrm{std}(\widetilde{\omega_{20km}})$), we find that the mesoscale vorticity perturbation first experiences a fast spin-up stage and then an exponential growth stage. To robustly predict the vortex strength evolution, we need to understand the mesoscale instability and how much vorticity perturbation is produced at the spin-up stage, which determines the initial amplitude for the mesoscale instability.

At the spin-up stage, we find that the vorticity growth is determined mainly by the random stretching of planetary vorticity by deep convection. This renders a wide spectrum of perturbation in the wavenumber space and leads to a universal relation: $\mathrm{std}(\widetilde{\omega_{20km}}) \sim R^{1/2}$. Here R (unit: mm) is the domain-averaged accumulated rainfall, which measures the accumulated number of clouds and, therefore, the number of vortex stretching events. The R is a rescaled time coordinate vital for revealing this universal relation.

The diagnosed spectral growth rate shows a most unstable wavelength at the exponential growth stage. For the reference test, it is around 150 km. While the long-wavelength cutoff is generally attributed to the control of the vortex size by the Rossby deformation radius (e.g., Charney and Eliassen 1964), what causes the short-wavelength cutoff here? In this paper, we design mechanism-denial numerical experiments to show that cloud-scale dynamics provide a smoothing effect with at least two factors:

- First, the spread of convective activity by cold pools. We find that the diagnosed most unstable wavelength increases as the sub-cloud rain evaporation rate increases.

- Second, the nonlocal longwave radiative heating induced by the anvil clouds. Because an anvil cloud is wider than an updraft, the column moistening caused by the radiation-induced secondary circulation is more widespread than the updraft. Instead of directly modifying the cloud microphysics, we perform cloud-permitting simulations that horizontally smooth the longwave radiative heating tendency with a Gaussian filter to mimic the radiative effect of wider anvil clouds. The filter does increase the most unstable wavelength, which indirectly confirms this hypothesis.

The strong sensitivity to cloud-scale dynamics inspires us to modify the precipitation-vapor relationship to be nonlocal by letting the diabatic heating rate be proportional to the Gaussian-filtered free-tropospheric vapor content. The filter length L_c is a bulk measure of the convective spreading by cold pools and the nonlocal longwave heating. Adding the filter to a linear stability analysis of the hydrostatic Boussinesq system truncated to the first baroclinic mode and including an equation for the free-tropospheric vapor content, we obtain an analytical expression of the spectral growth rate (26). Its shape agrees well with the simulations after fitting a few parameters. The most unstable wavelength is proportional to $(L_R L_c)^{1/2}$. Here L_R is the effective Rossby deformation radius calculated with the gravity wave speed of convectively coupled gravity waves. They move slower than dry gravity waves. Even a small change of L_c can significantly influence the most unstable wavelength $(L_R L_c)^{1/2}$, because $L_c \ll L_R$. This explains the strong sensitivity of the vortex size to L_c observed in our Group 4 experiments. Thus, the cloud microphysics (e.g., sub-cloud rain evaporation and ice sublimation rate), which modulates the cloud dynamics (e.g., cold pool strength and anvil cloud size) and therefore L_c, may have an important influence on the size of an early-stage mesoscale convective vortex.

The theory is still far from complete. In particular, the four parameters τ_d, τ, L_R, and L_c are still fitted in calculating the theoretical spectral growth rate. We list a few possible research directions:

- The influence of ice sublimation rate on τ and L_c can be studied, and the result could be compared with the Group 4 experiments where the longwave heating rate is smoothed.

- A theoretical model on the spread of convective activity by cold pools is needed to justify the choice of L_c. In addition, the anvil cloud is also a gravity current, just like a cold pool. Is there any physical factor that can modify the size of an anvil cloud and a cold pool at the same time?

- We consider the experiments reported in this paper to be in the moisture-radiation-instability regime. If the parameter RAD and therefore the cloud radiative feedback parameter ϵ_{rad} takes a higher value, could c_e^2 drop below zero and make the system transition to the wave-CISK-radiation instability? An interesting problem is the transition behavior of the system near $c_e^2 = 0$.

- A linear stability analysis with two vertical modes can be considered. We also observed amplifying gravity waves in the experiments where f or $\mathrm{E_v}$ is small [10]. Could the stationary instability (vortices) and the oscillatory instability (waves) be unified in one theoretical framework?

Acknowledgments. We are grateful to Prof. Da Yang at UC Davis, Prof. Zhaohua Wu at Florida State University, and Dr. Bolei Yang at Peking University for helpful discussions. We thank Stanford University and Stanford Research Computing Center for providing funding and computational resources.

Data availability statement. The supplemental material includes a derivation note, tables of mathematical symbols, the MATLAB code for postprocessing, the Fortran code for performing the radiative filter in CM1, and the movie version of Figs. 8-11 from day 0 to day 20.

APPENDIX

The wave-CISK-radiation instability with convective spreading

In this appendix, we consider the $c_e^2 < 0$ case, where the latent heating and cloud-longwave radiative heating induced by an updraft overcome the stable stratification and cause instability. Brenowitz et al. (2016) have performed a numerical linear stability analysis of non-rotating convectively coupled gravity waves with a spatial filter on the convergence field. Due to the complexity of their model, they did not analytically calculate the expression for the most unstable wavelength. We will show that the wave-CISK-radiation instability cannot fit the growth rate (σ) of our Group 1 experiments where σ is insensitive to f but is much smaller than f at the same time.

To highlight the wave-CISK-radiation instability, we remove the moisture-radiation feedback by setting $\alpha = 0$. The buoyancy equation is modified to:

$$\frac{\partial b}{\partial t} = -N^2 w + \beta(1+\epsilon_{rad})N^2 \widetilde{w_{L_c}} - \frac{b}{\tau_d}. \tag{A1}$$

---

[10] See the movies of the $f = 0.25 \times 10^{-4}\ \mathrm{s^{-1}}$ and $\mathrm{E_v} = 0.5$ tests in the supplemental material.

This, together with (11)-(14), constitute the governing equation. Note that there is no vapor equation. Substituting in the normal mode (19), we get:

$$
\begin{aligned}
\sigma &= \left(K^2 c_e^2 - f^2\right)^{1/2} - \frac{1}{\tau_d} \\
&= \left\{K^2 c^2 \left[\beta(1+\epsilon_{rad}) e^{-\frac{K^2 L_c^2}{4}} - 1\right] - f^2\right\}^{1/2} - \frac{1}{\tau_d} \\
&\approx \left\{K^2 c^2 \left[\beta(1+\epsilon_{rad}) - \beta(1+\epsilon_{rad}) \frac{K^2 L_c^2}{4} - 1\right] - f^2\right\}^{1/2} - \frac{1}{\tau_d} \\
&= \left\{-\frac{\beta c^2 L_c^2}{4} \left[K^2 - \frac{2}{L_c^2}\left(\frac{\beta(1+\epsilon_{rad})-1}{\beta(1+\epsilon_{rad})}\right)\right]^2 + \frac{\beta(1+\epsilon_{rad})c^2}{L_c^2}\left(\frac{\beta(1+\epsilon_{rad})-1}{\beta(1+\epsilon_{rad})}\right)^2 - f^2\right\}^{1/2} - \frac{1}{\tau_d}.
\end{aligned}
\tag{A2}
$$

Here we have used Taylor expansion to simplify the filter term: $e^{-\frac{K^2 L_c^2}{4}} \approx 1 - K^2 L_c^2/4$, which is valid for $KL_c \ll 1$. Equation (A2) shows a convex spectral growth rate. Its most unstable wavenumber K_m and growth rate σ_m obey:

$$
K_m = \frac{1}{L_c}\left\{\frac{2\left[\beta(1+\epsilon_{rad})-1\right]}{\beta(1+\epsilon_{rad})}\right\}^{1/2}, \tag{A3}
$$

$$
\sigma_m = \left\{\underbrace{\frac{\beta(1+\epsilon_{rad})c^2}{L_c^2}\left[\frac{\beta(1+\epsilon_{rad})-1}{\beta(1+\epsilon_{rad})}\right]^2}_{\sigma_{m0}^2} - f^2\right\}^{1/2} - \frac{1}{\tau_d}, \tag{A4}
$$

where $\sigma_{m0} \equiv [\beta(1+\epsilon_{rad})/2]^{1/2} K_m c$ (unit: s^{-1}) is a constant parameter in (A4) that is introduced to make the explanation neater. Like the moisture-radiation instability, a larger convective spreading length scale L_c makes K_m and σ_m smaller. However, the sensitivity to f is quite different. First, the K_m in the wave-CISK-radiation instability is solely determined by L_c. In contrast, the K_m of the moisture-radiation instability is determined by $(L_c L_R)^{1/2}$. Because the sensitivity of K_m to f (and therefore L_R) is unclear in the diagnosed growth rate (Fig. 14a), we do not further compare the most unstable wavelength.

The most striking difference is the change of σ_m with f. Figure 14a shows that the diagnosed most unstable growth rate σ_m has two features:

- The σ_m only decreases slightly with f between $f = 0.25 \times 10^{-4}$ s^{-1}, $f = 0.5 \times 10^{-4}$ s^{-1}, and $f = 1 \times 10^{-4}$ s^{-1}.
- The σ_m is around 0.75 day^{-1} ($\approx 0.09 \times 10^{-4}$ s^{-1}), which is much smaller than any of the three Coriolis parameters.

These two conditions cannot be satisfied simultaneously by (A4). For σ_m to be insensitive to f, $\sigma_m + \frac{1}{\tau_d}$ must be much larger than f:

$$\sigma_m + \frac{1}{\tau_d} \approx \sigma_{m0} \gg f. \tag{A5}$$

This contradicts the simulation results where $\sigma_m \ll f$ and no known damping factor could make $\tau_d \ll f^{-1} \sim 0.12$ days. Thus, we consider that our numerical experiments do not lie in the regime of wave-CISK-radiation instability.

References

Ahmed, F., and J. D. Neelin, 2019: Explaining scales and statistics of tropical precipitation clusters with a stochastic model. *J. Atmos. Sci.*, **76 (10)**, 3063–3087.

Benzi, R., M. Colella, M. Briscolini, and P. Santangelo, 1992: A simple point vortex model for two-dimensional decaying turbulence. *Phys. Fluids*, **4 (5)**, 1036–1039.

Bjerknes, J., 1938: Saturated-adiabatic ascent of air through dry-adiabatically descending environment. *Quart. J. Roy. Meteor. Soc.*, **64**, 325–330.

Boubnov, B., and G. Golitsyn, 1986: Experimental study of convective structures in rotating fluids. *J. Fluid Mech.*, **167**, 503–531.

Brenowitz, N., Y. Frenkel, and A. Majda, 2016: Non-local convergence coupling in a simple stochastic convection model. *Dyn. Atmos. Oceans*, **74**, 30–49.

Bretherton, C. S., P. N. Blossey, and M. Khairoutdinov, 2005: An energy-balance analysis of deep convective self-aggregation above uniform SST. *J. Atmos. Sci.*, **62 (12)**, 4273–4292.

Bretherton, C. S., M. E. Peters, and L. E. Back, 2004: Relationships between water vapor path and precipitation over the tropical oceans. *J. Climate*, **17 (7)**, 1517–1528.

Bryan, G. H., and J. M. Fritsch, 2002: A benchmark simulation for moist nonhydrostatic numerical models. *Mon. Wea. Rev.*, **130 (12)**, 2917–2928.

Bryan, G. H., and R. Rotunno, 2009: The maximum intensity of tropical cyclones in axisymmetric numerical model simulations. *Mon. Wea. Rev.*, **137 (6)**, 1770–1789.

Carstens, J. D., and A. A. Wing, 2020: Tropical cyclogenesis from self-aggregated convection in numerical simulations of rotating radiative-convective equilibrium. *J. Adv. Model. Earth Syst.*, **12 (5)**, e2019MS002 020.

Carstens, J. D., and A. A. Wing, 2022: A spectrum of convective self-aggregation based on background rotation. *J. Adv. Model. Earth Syst.*, e2021MS002860.

Chandrasekhar, S., 1961: *Hydrodynamic and hydromagnetic stability*. Courier Corporation.

Charney, J. G., and A. Eliassen, 1964: On the growth of the hurricane depression. *J. Atmos. Sci.*, **21 (1)**, 68–75.

Clough, S., M. Shephard, E. Mlawer, J. Delamere, M. Iacono, K. Cady-Pereira, S. Boukabara, and P. Brown, 2005: Atmospheric radiative transfer modeling: A summary of the aer codes. *J. Quant. Spectrosc. Radiat. Transf.*, **91 (2)**, 233–244.

Craig, G., and J. Mack, 2013: A coarsening model for self-organization of tropical convection. *J. Geophys. Res.*, **118 (16)**, 8761–8769.

Davis, C. A., 2015: The formation of moist vortices and tropical cyclones in idealized simulations. *J. Atmos. Sci.*, **72 (9)**, 3499–3516.

Derbyshire, S., I. Beau, P. Bechtold, J.-Y. Grandpeix, J.-M. Piriou, J.-L. Redelsperger, and P. Soares, 2004: Sensitivity of moist convection to environmental humidity. *Quart. J. Roy. Meteor. Soc.*, **130 (604)**, 3055–3079.

Dunkerton, T., M. Montgomery, and Z. Wang, 2009: Tropical cyclogenesis in a tropical wave critical layer: easterly waves. *Atmos. Chem. Phys.*, **9 (15)**.

Dunkerton, T. J., and F. X. Crum, 1991: Scale selection and propagation of wave-cisk with conditional heating. *Journal of the Meteorological Society of Japan. Ser. II*, **69 (4)**, 449–458.

Emanuel, K., A. A. Wing, and E. M. Vincent, 2014: Radiative-convective instability. *J. Adv. Model. Earth Syst.*, **6 (1)**, 75–90.

Emanuel, K. A., and Coauthors, 1994: *Atmospheric convection*. Oxford University Press on Demand.

Fu, H., and M. O'Neill, 2022: A theory of cloud spacing for equilibrium deep convection. *EarthArXiv*.

Fu, H., and M. O'Neill, 2021: The role of random vorticity stretching in tropical depression genesis. *J. Atmos. Sci.*, **78 (12)**, 4143–4168.

Fu, H., and S. Sun, 2021: On the asymmetry of cyclones and anticyclones in the cellular regime of rotating rayleigh-bénard convection. *EarthArXiv*.

Fuchs, Ž., and D. J. Raymond, 2002: Large-scale modes of a nonrotating atmosphere with water vapor and cloud–radiation feedbacks. *J. Atmos. Sci.*, **59 (10)**, 1669–1679.

Fuchs, Ž., and D. J. Raymond, 2017: A simple model of intraseasonal oscillations. *J. Adv. Model. Earth Syst.*, **9 (2)**, 1195–1211.

Grandpeix, J.-Y., and J.-P. Lafore, 2010: A density current parameterization coupled with emanuel's convection scheme. part i: The models. *J. Atmos. Sci.*, **67 (4)**, 881–897.

Gray, W. M., 1998: The formation of tropical cyclones. *Meteorology and atmospheric physics*, **67 (1-4)**, 37–69.

Haertel, P. T., and G. N. Kiladis, 2004: Dynamics of 2-day equatorial waves. *J. Atmos. Sci.*, **61 (22)**, 2707–2721.

Hottovy, S., and S. N. Stechmann, 2015: A spatiotemporal stochastic model for tropical precipitation and water vapor dynamics. *J. Atmos. Sci.*, **72 (12)**, 4721–4738.

Jeevanjee, N., and D. M. Romps, 2013: Convective self-aggregation, cold pools, and domain size. *Geophys. Res. Lett.*, **40 (5)**, 994–998.

Jensen, G. G., R. Fiévet, and J. O. Haerter, 2022: The diurnal path to persistent convective self-aggregation. *J. Adv. Model. Earth Syst.*, e2021MS002923.

Jiménez, P. A., J. Dudhia, J. F. González-Rouco, J. Navarro, J. P. Montávez, and E. García-Bustamante, 2012: A revised scheme for the wrf surface layer formulation. *Mon. Wea. Rev.*, **140 (3)**, 898–918.

Khairoutdinov, M., and K. Emanuel, 2013: Rotating radiative-convective equilibrium simulated by a cloud-resolving model. *J. Adv. Model. Earth Syst.*, **5 (4)**, 816–825.

Langhans, W., and D. M. Romps, 2015: The origin of water vapor rings in tropical oceanic cold pools. *Geophys. Res. Lett.*, **42 (18)**, 7825–7834.

Lindzen, R. S., 1974: Wave-cisk in the tropics. *J. Atmos. Sci.*, **31 (1)**, 156–179.

Liu, C., and M. W. Moncrieff, 2004: Effects of convectively generated gravity waves and rotation on the organization of convection. *J. Atmos. Sci.*, **61 (17)**, 2218–2227.

Liu, Y., Z.-M. Tan, and Z. Wu, 2019: Noninstantaneous wave-CISK for the interaction between convective heating and low-level moisture convergence in the tropics. *J. Atmos. Sci.*, **76 (7)**, 2083–2101.

Mapes, B. E., 1993: Gregarious tropical convection. *J. Atmos. Sci.*, **50 (13)**, 2026–2037.

Mapes, B. E., 1997: Equilibrium vs. activation control of large-scale variations of tropical deep convection. *The physics and parameterization of moist atmospheric convection*, Springer, 321–358.

Mapes, B. E., 2000: Convective inhibition, subgrid-scale triggering energy, and stratiform instability in a toy tropical wave model. *J. Atmos. Sci.*, **57 (10)**, 1515–1535.

Meyer, B., and J. O. Haerter, 2020: Mechanical forcing of convection by cold pools: Collisions and energy scaling. *J. Adv. Model. Earth Syst.*, **12 (11)**, e2020MS002 281.

Morrison, H., J. Curry, and V. Khvorostyanov, 2005: A new double-moment microphysics parameterization for application in cloud and climate models. part i: Description. *J. Atmos. Sci.*, **62 (6)**, 1665–1677.

Muller, C. J., and D. M. Romps, 2018: Acceleration of tropical cyclogenesis by self-aggregation feedbacks. *Proc. Natl. Acad. Sci. (USA)*, **115 (12)**, 2930–2935.

Narenpitak, P., C. S. Bretherton, and M. F. Khairoutdinov, 2020: The role of multiscale interaction in tropical cyclogenesis and its predictability in near-global aquaplanet cloud-resolving simulations. *J. Atmos. Sci.*, **77 (8)**, 2847–2863.

Neelin, J. D., and I. M. Held, 1987: Modeling tropical convergence based on the moist static energy budget. *Mon. Wea. Rev.*, **115 (1)**, 3–12.

Nissen, S. B., and J. O. Haerter, 2021: Circling in on convective self-aggregation. *J. Geophys. Res.*, **126 (20)**, e2021JD035 331.

Nolan, D. S., E. D. Rappin, and K. A. Emanuel, 2007: Tropical cyclogenesis sensitivity to environmental parameters in radiative–convective equilibrium. *Quart. J. Roy. Meteor. Soc.*, **133 (629)**, 2085–2107.

Ooyama, K., 1969: Numerical simulation of the life cycle of tropical cyclones. *J. Atmos. Sci.*, **26 (1)**, 3–40.

Ooyama, K. V., 1982: Conceptual evolution of the theory and modeling of the tropical cyclone. *J Meteorol Soc Jpn*, **60 (1)**, 369–380.

Patrizio, C. R., and D. A. Randall, 2019: Sensitivity of convective self-aggregation to domain size. *J. Adv. Model. Earth Syst.*, **11 (7)**, 1995–2019.

Ramírez Reyes, A., and D. Yang, 2021: Spontaneous cyclogenesis without radiative and surface-flux feedbacks. *J. Atmos. Sci.*, **78 (12)**, 4169–4184.

Raymond, D. J., and S. L. Sessions, 2007: Evolution of convection during tropical cyclogenesis. *Geophys. Res. Lett.*, **34 (6)**.

Raymond, D. J., S. L. Sessions, and Ž. Fuchs, 2007: A theory for the spinup of tropical depressions. *Quart. J. Roy. Meteor. Soc.*, **133 (628)**, 1743–1754.

Raymond, D. J., S. L. Sessions, A. H. Sobel, and Ž. Fuchs, 2009: The mechanics of gross moist stability. *J. Adv. Model. Earth Syst.*, **1 (3)**.

Romps, D. M., 2014: Rayleigh damping in the free troposphere. *J. Atmos. Sci.*, **71 (2)**, 553–565.

Ruppert, J. H., 2022: The stratiform pathway of cloud–radiation feedback in tropical convection. *35th Conference on Hurricanes and Tropical Meteorology*, AMS.

Ruppert, J. H., A. A. Wing, X. Tang, and E. L. Duran, 2020: The critical role of cloud–infrared radiation feedback in tropical cyclone development. *Proc. Natl. Acad. Sci. (USA)*, **117 (45)**, 27 884–27 892.

Schecter, D. A., and T. J. Dunkerton, 2009: Hurricane formation in diabatic ekman turbulence. *Quart. J. Roy. Meteor. Soc.*, **135 (641)**, 823–838.

Seeley, J. T., N. Jeevanjee, W. Langhans, and D. M. Romps, 2019: Formation of tropical anvil clouds by slow evaporation. *Geophys. Res. Lett.*, **46 (1)**, 492–501.

Sobel, A. H., J. Nilsson, and L. M. Polvani, 2001: The weak temperature gradient approximation and balanced tropical moisture waves. *J. Atmos. Sci.*, **58 (23)**, 3650–3665.

Tompkins, A. M., 2001: Organization of tropical convection in low vertical wind shears: The role of cold pools. *J. Atmos. Sci.*, **58 (13)**, 1650–1672.

Vallis, G., G. Shutts, and M. Gray, 1997: Balanced mesoscale motion and stratified turbulence forced by convection. *Quart. J. Roy. Meteor. Soc.*, **123 (542)**, 1621–1652.

Vallis, G. K., 2017: *Atmospheric and oceanic fluid dynamics*. Cambridge University Press.

Wang, S., and A. H. Sobel, 2022: A unified moisture mode theory for the madden–julian oscillation and the boreal summer intraseasonal oscillation. *J. Climate*, **35 (4)**, 1267–1291.

Wang, Y., C. A. Davis, and Y. Huang, 2019: Dynamics of lower-tropospheric vorticity in idealized simulations of tropical cyclone formation. *J. Atmos. Sci.*, **76 (3)**, 707–727.

Windmiller, J. M., and G. C. Craig, 2019: Universality in the spatial evolution of self-aggregation of tropical convection. *J. Atmos. Sci.*, **76 (6)**, 1677–1696.

Wing, A. A., S. J. Camargo, and A. H. Sobel, 2016: Role of radiative–convective feedbacks in spontaneous tropical cyclogenesis in idealized numerical simulations. *J. Atmos. Sci.*, **73 (7)**, 2633–2642.

Wing, A. A., and K. A. Emanuel, 2014: Physical mechanisms controlling self-aggregation of convection in idealized numerical modeling simulations. *J. Adv. Model. Earth Syst.*, **6 (1)**, 59–74.

Wu, Z., D. S. Battisti, and E. Sarachik, 2000: Rayleigh friction, newtonian cooling, and the linear response to steady tropical heating. *J. Atmos. Sci.*, **57 (12)**, 1937–1957.

Yang, B., and Z.-M. Tan, 2020: Interactive radiation accelerates the intensification of the midlevel vortex for tropical cyclogenesis. *J. Atmos. Sci.*, **77 (12)**, 4051–4065.

Yang, D., 2020: A shallow water model for convective self-aggregation. *J. Atmos. Sci.*, 1–41.

Yang, Q., L. R. Leung, Z. Feng, F. Song, and X. Chen, 2021: A simple lagrangian parcel model for the initiation of summertime mesoscale convective systems over the central united states. *J. Atmos. Sci.*, **78 (11)**, 3537–3558.